

# Calibrating cosmological radiative transfer simulations with Ly $\alpha$ forest data: Evidence for large spatial UV background fluctuations at $z \sim 5.6 - 5.8$ due to rare bright sources

Jonathan Chardin<sup>1\*</sup>, Martin G. Haehnelt<sup>1</sup>, Dominique Aubert<sup>2</sup> and Ewald Puchwein<sup>1</sup>

<sup>1</sup>*Kavli Institute for Cosmology and Institute of Astronomy, Madingley Road, Cambridge CB3 0HA*

<sup>2</sup>*Observatoire Astronomique de Strasbourg, Université de Strasbourg, CNRS UMR 7550, 11 rue de l'Université, F-67000 Strasbourg, France*

Accepted / Received

## ABSTRACT

We calibrate here cosmological radiative transfer simulations with ATON/RAMSES with a range of measurements of the Ly $\alpha$  opacity from QSO absorption spectra. We find the Ly $\alpha$  opacity to be very sensitive to the exact timing of hydrogen reionisation. Models reproducing the measured evolution of the mean photoionisation rate and average mean free path reach overlap at  $z \sim 7$  and predict an accelerated evolution of the Ly $\alpha$  opacity at  $z > 6$  consistent with the rapidly evolving luminosity function of Ly $\alpha$  emitters in this redshift range. Similar to "optically thin" simulations our full radiative transfer simulations fail, however, to reproduce the high-opacity tail of the Ly $\alpha$  opacity PDF at  $z > 5$ . We argue that this is due to spatial UV fluctuations in the post-overlap phase of reionisation on substantially larger scales than predicted by our source model, where the ionising emissivity is dominated by large numbers of sub-L $_{\star}$  galaxies. We further argue that this suggests a significant contribution to the ionising UV background by much rarer bright sources at high redshift.

**Key words:** Cosmology: theory - Methods: numerical - diffuse radiation - IGM: structure - Galaxy: evolution - quasars: general

## 1 INTRODUCTION

The Ly $\alpha$  forest is a valuable probe of the underlying matter density field, as well as of the temperature and ionisation state of the Inter-Galactic-Medium (IGM) at high redshift (see Rauch 1998, Meiksin 2009 for reviews). There is strong evidence that, despite a significantly increased effective Ly $\alpha$  optical depth, even the highest redshift QSOs at  $z \sim 6$  still probe the post-reionisation highly-ionised IGM (Bolton & Haehnelt 2007, *cf.* Lidz et al. 2006 and Mesinger 2010), apart from perhaps the notable  $z = 7.085$  QSO ULAS J1120+0641 which appears to show signs of a red damping wing suggesting a volume fraction of neutral hydrogen of 10% or more (Fan et al. 2006, Mortlock et al. 2011 and Bolton et al. 2011), but see Bosman & Becker (2015) (*in prep*) for a recent reassessment of the significance of the weak Ly $\alpha$  emission of ULAS J1120+0641.

This is in good agreement with the constraints on the reionisation history by the CMB which also suggests that most of hydrogen in the Universe has been reionised earlier than  $z \sim 6$ , even though the most recent Planck (Planck Collaboration et al. 2015) measurements suggest a somewhat later (end of) reionisation than earlier CMB measurements.

The accelerating evolution of the Ly $\alpha$  optical depth at  $z > 5$  (Fan et al. 2006) and the apparent rapid decrease of the observed Ly $\alpha$  emission of high-redshift galaxies (Bolton & Haehnelt 2013 and Dijkstra et al. 2014) also suggest that at  $z \sim 6$  we are witnessing the final stages of the reionisation process (Ouchi et al. 2010, Kashikawa et al. 2011, Pentericci et al. 2011, Treu et al. 2013, Caruana et al. 2014, Faisst et al. 2014, Pentericci et al. 2014, Konno et al. 2014 and Choudhury et al. 2014). This has been further corroborated by a recent accurate measurement of Ly $\alpha$  optical depth PDF at  $4 < z < 6$  by Becker et al. (2015) based on a large sample of high-quality high-redshift QSO absorption spectra.

Simulation of the hydrogen Ly $\alpha$  forest at  $z < 5$  have

\*E-mail: jc@ast.cam.ac.uk

mostly been performed assuming that hydrogen is already highly ionised, that the Universe can be assumed to be optically thin for hydrogen ionising radiation and that radiative transfer effects can be neglected. The UV background in these simulations is assumed to be spatially homogeneous as in widely used spectral synthesis models of the UV background (Haardt & Madau 1996, Haardt & Madau 2001, Haardt & Madau 2012).

Such simulations have been used widely to infer the hydrogen photoionisation rate by rescaling the optical depth in the simulations such that it matches that observed (Rauch et al. 1997, Theuns et al. 1998, Bolton et al. 2005, Bolton & Haehnelt 2007, Faucher-Giguère et al. 2008a, Faucher-Giguère et al. 2008b, Calverley et al. 2011 and Becker & Bolton 2013). When comparing such simulations to their measurements of the Ly $\alpha$  optical depth PDF Becker et al. (2015) reported rapidly increasing deviations for the high opacity tail of the PDF at  $z > 5$  and interpreted that being due to spatial fluctuations in the photoionisation rate in the post-overlap phase of reionisation as expected in models for inhomogeneous reionisation (Miralda-Escudé et al. 2000).

More detailed modelling of this clearly requires full cosmological radiative transfer simulations. Most cosmological radiative transfer simulations have concentrated on the large scale topology of reionisation (Gnedin & Abel 2001, Razoumov et al. 2002, Iliev et al. 2006, Lidz et al. 2007, Trac & Cen 2007, Aubert & Teyssier 2008, Finlator et al. 2009, Petkova & Springel 2009, Aubert & Teyssier 2010, Chardin et al. 2012) in rather large simulation boxes. Fully understanding the growth of ionised regions requires, however, not only an accurate modelling of the large scale distribution of the sources of ionising radiation but also of the sinks of ionising radiation as is being increasingly realised (Miralda-Escudé et al. 2000, Furlanetto & Oh 2005, Furlanetto & Mesinger 2009, Choudhury et al. 2009, McQuinn et al. 2011, Kaurov & Gnedin 2013, Gnedin 2014, Gnedin & Kaurov 2014, Choudhury et al. 2014 and Mesinger et al. 2015).

This makes accurate cosmological radiative transfer simulations numerically extremely demanding in terms of dynamic range and hybrid techniques to treat small and large scale separately are being developed (Mesinger & Furlanetto 2007, Choudhury et al. 2014 and Mesinger et al. 2015).

Accurate modelling of the sinks of ionising radiation is particularly important for modelling of Ly $\alpha$  forest data and this is the main focus of the paper here (see also Petkova & Springel 2009). For this, we use here a suite of rather high-resolution hydro-dynamical RAMSES simulations (Teyssier 2002) post-processed with the GPU-based radiative transfer code ATON (Aubert & Teyssier 2008). Note that the box size of our simulation are smaller than those of many other reionisation simulations in order to properly resolve regions optically thick to ionising radiation in the post-overlap phase.

The paper is organized as follows: In section 2, we present the main features of the simulations performed in the context of this work. In section 3, we present our results first for the evolution of global quantities in the simulation and second for the evolution of Lyman-alpha forest statistics in our different model. We discuss our results and make predictions for the evolution of the ionising UV background in section 3.2 and we give our conclusions and

present prospects concerning further work in section 4. Our simulations assume the following cosmological parameter (as derived from the 2013 Planck temperature power spectrum data alone, Planck Collaboration et al. 2014):  $\Omega_m = 0.3175$ ,  $\Omega_\Lambda = 0.6825$ ,  $\Omega_b = 0.048$ ,  $h = 0.6711$ ,  $\sigma_8 = 0.8344$ , and  $n_s = 0.9624$ .

## 2 NUMERICAL SIMULATIONS

We briefly describe here our modelling of the spatial distribution of matter with cosmological hydro-simulations with the code RAMSES and the radiative transfer calculation performed as a post-processing step on the hydrodynamic simulation outputs with the code ATON. We will take particular care to model the Ly $\alpha$  forest in QSO absorption spectra during the post-overlap phase of reionization. We benchmark our modelling against the widely used (homogeneous) UV background model of Haardt & Madau (2012) (HM2012 hereafter), which takes into account a broad set of recent data.

### 2.1 Cosmological hydrosimulations with RAMSES

We have performed cosmological hydro-simulations with the adaptive mesh refinement code RAMSES (Teyssier 2002). In RAMSES the gas dynamics is solved with a 2nd order Godunov scheme combined with a HLLC Riemann solver. The collisionless dynamics of the dark matter (DM) is represented by DM particles and the gravitational potential is calculated with a multi-resolution multi-grid solver. Initial conditions were produced with MUSIC (Hahn & Abel 2013).

Star formation is included following the prescription of Rasera & Teyssier (2006). The star formation recipe assumes that above a baryon over-density of  $\delta \sim 50$  gas transforms into stars of constant mass with efficiency  $\epsilon = 0.01$  per free fall time. We do not include stellar or AGN feedback and metal enrichment has also not been included (see Bauer et al. 2015 for a recent cosmological radiative transfer simulation based on the Illustris simulation with AGN and stellar feedback tuned to form a realistic galaxy population).

The usual primordial cooling processes for hydrogen and helium are taken into account: collisional ionisation cooling, recombination cooling, dielectronic recombination cooling, collisional excitation cooling, bremsstrahlung and inverse Compton cooling (see Theuns et al. 1998). Simulation outputs are generated every 40 Myrs from  $z \sim 30$  to  $z \sim 2$  which results in 80 outputs for each of the simulations described further in section 2.4.

### 2.2 Radiative transfer in post-processing with ATON

The radiative transfer calculations have been performed as a post-processing step with the ATON code. ATON is described in Aubert & Teyssier (2008) and has been mainly used to model hydrogen reionisation (Aubert & Teyssier 2010, Chardin et al. 2012 and Chardin et al. 2014) and in particular the reionisation of our Local Group of galaxies (Ocvirk et al. 2013 and Ocvirk et al. 2014). ATON employs a moment-based description of the radiative transfer equation, based on the M1 approximation that provides a simple

and local closure relation between radiative pressure and radiative energy density. The code takes advantage of GPU acceleration to solve the equations explicitly in conservative form while satisfying a very strict Courant condition, i.e.  $\Delta t < c \Delta x/3$ , where  $\Delta t$  is the time step,  $\Delta x$  the cell size and  $c$  the speed of light.

Note that the radiative transfer in ATON uses the actual speed of light  $c$  and not a reduced speed of light approximation (see Gnedin & Abel 2001 and Bauer et al. 2015). Note further that we have not used here ATON’s ability to follow photons with a range of frequencies. We have used instead the computationally cheaper options of tracing only monochromatic ionising photons with energy of 20.27 eV, approximately the mean photon energy of a 50000 K blackbody spectrum (see also Baek et al. 2009).

The radiative transfer is performed on a grid with resolution equal to that of the coarse base grid of our RAMSES simulations. Note that ATON is not able to follow the AMR structure of RAMSES and that the RAMSES simulations used do not include any level of mesh refinement. Note further that recently a version of this radiative transfer scheme has been directly implemented in RAMSES (Rosdahl et al. 2013) that couples self-consistently radiative forces to the dynamics of the gas. This version is, however, computationally much more expensive and we do not use it here. During post-processing the density and temperature fields from the RAMSES simulations are updated within the radiative transfer calculation every 40 Myrs corresponding to the frequency of hydrodynamic simulation outputs obtained with RAMSES.

## 2.3 Modelling of ionising sources

### 2.3.1 Optically thin simulations with the HM2012 UV background model

Extensive previous modelling of Ly $\alpha$  forest data by some of the authors was based on hydrodynamical simulations with P-GADGET3 (an improved version of GADGET2 last described in Springel 2005) neglecting radiative transfer. To make contact to this work we have first compared “optically thin” RAMSES simulations with a homogeneous UV background with comparable P-GADGET3 simulations to make sure that we obtain consistent results.

For this purpose, we have implemented the latest version of the UV background of HM2012 in the RAMSES code. In the optically thin approximation at any given time the photoionisation and photoheating rates are independent of location (and density). Every part of the simulation sees the same UV background intensity. The time evolution of the space averaged UV background intensity is calculated by solving a global radiative transfer equation with an empirical opacity model and a source function based on the observed UV luminosity function of quasar and star forming galaxies. The HM2012 background model calculated in this way should give a reasonable approximation to the spatially averaged photoionisation rates, especially once the Universe is fully ionised (see Puchwein et al. 2015 for a recent discussion). By construction, it will however not be able to describe the growth of individual HII regions before overlap and the persistence of spatial amplitude fluctuation in the

UV flux and therefore photoionisation rate for some time after overlap.

We will later compare such optically thin simulations to our full cosmological radiative transfer simulation with ATON where the ionising radiation is propagated from discrete sources into the surrounding IGM. Note that we do not try to model the ionising radiation from star formation in our simulation self-consistently (other than, e.g. Bauer et al. 2015), but that we assume an ionising volume emissivity scaled to that assumed in the HM2012 UV background model and identify the dark matter haloes in our simulations as the ionising sources. The dark matter haloes are identified with the HOP halo finder (Eisenstein & Hut 1998) with a minimal halo mass consisting of 10 particles, corresponding to the minimal masses reported in Tables 1 and 2. We assume that dark matter haloes above our mass thresholds act as ionising sources with emissivities proportional to halo mass  $M$  similar to the assumptions in Iliev et al. (2006),

$$\dot{N}_\gamma(z) = \alpha(z)M. \quad (1)$$

Note here that simple models where the UV luminosity is proportional to halo mass appear to fit (UV) luminosity functions of high-redshift galaxies remarkably well (see Trenti et al. 2010). We will investigate this further in Appendix B.

### 2.3.2 Choosing the ionising emissivity for the ATON simulations

In order to obtain a realistic post-overlap Ly $\alpha$  forest and for an easier comparison with our optically thin simulations we have scaled our emissivities in the ATON simulations such that the volume average are close to that of the HM2012 model, shown as the black solid curve in Fig. 1. The required re-scaling will be discussed in detail below.

Note again that we thereby have not tried to match the space density of sources in the HM2012 model in our ATON simulations, but just the redshift evolution of the integrated emissivity. For a given population of DM haloes identified as ionising sources this fixes then the evolution of the efficiency parameter  $\alpha(z)$  of equation 1. The HM2012 model uses a simple escape fraction to model the fraction of ionising photons escaping galaxies,

$$\langle f_{\text{esc}} \rangle = 1.8 \times 10^{-4} (1+z)^{3.4}. \quad (2)$$

As ATON is modelling the escape of photons from the source positions explicitly we have to account for this and boost the escaping ionising emissivity compared to “optically thin” simulations with a spatial homogeneous UV background model like HM2012 by a resolution dependent factor that accounts for the recombinations in the host haloes of our ionising sources. As we will see later “recombination” boost factors in the range  $\sim 1.05 - 2$  gave reasonable reionisation histories. Note that these boost factors should be equal to the inverse of the escape fraction in the HM2012 background model if our simulations were able to correctly model the escape of ionising photons from real galaxies. That these factors are significantly smaller just means that they are clearly and not surprisingly not able to do this. As we will see later the redshift evolution of the ionising emissivity of HM2012 does not get the rather flat evolution of the photoionisation rate at  $6 > z > 2$  as probed by Ly $\alpha$  forest

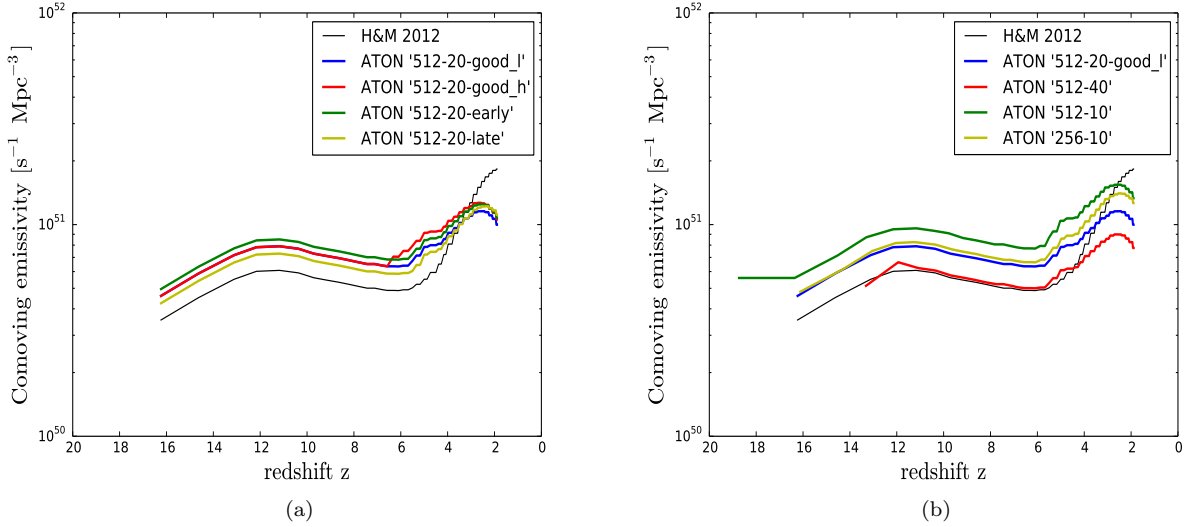


**Figure 1.** (a): Evolution of the comoving emissivity of ionising photons (in  $\text{s}^{-1}\text{Mpc}^{-3}$ ). The black solid curve represents the evolution of the emissivity from HM2012 integrated over all frequencies of ionising photons. The other curves show the ionising emissivities for the different ionisation histories studied with our ATON simulations. The emissivities have been re-scaled relative to the HM2012 model to reproduce observed photoionisation rates and to account for the resolution dependent recombinations in the host haloes of ionising sources. (b): same as (a) but for the simulations with different box sizes and resolution as described in the text.

data quite right. We were able to reproduce the  $\text{Ly}\alpha$  forest data and the inferred photoionisation rates by scaling the HM2012 ionising emissivities with a redshift dependent scaling factor as follows,

$$b(z) = \begin{cases} a = \text{const} & \text{if } z \geq z_1 \\ a \left[ \frac{z}{z_1} \right]^{\alpha_1} & \text{if } z_2 < z \leq z_1 \\ a \left[ \frac{z_2}{z_1} \right]^{\alpha_1} \left[ \frac{z}{z_2} \right]^{\alpha_2} & \text{if } z \leq z_2 \end{cases} \quad (3)$$

with suitable values of  $a$ ,  $z_1$ ,  $z_2$ ,  $\alpha_1$  and  $\alpha_2$  as shown in Tables 1 and 2. Unfortunately, there is no easy way round the resolution dependence of the number of recombinations occurring in the source haloes. It required some experimenting with the evolution of the ionising emissivity to obtain reasonable reionisation histories for which hydrogen reionisation is completed at about  $z \sim 6$  and the evolution of  $\Gamma(z)$  is close to the observations at redshifts below six. As the monochromatic GPU accelerated ATON radiative transfer code is gratifyingly fast (a speedup of 80-100 times compared to CPU-based implementation) we were able to do this by trial and error.

#### 2.4 The simulation set

We have run a suite of simulations in order to explore the convergence in terms of resolution and box size. We also varied the evolution of the ionising emissivity to study the effect of the timing of the overlap of HII regions on the  $\text{Ly}\alpha$  opacity PDF and the spatial fluctuation of the photoionisation rate in the post-overlap phase.

Our standard simulations are based on  $512^3$  RAMSES simulations and we have varied the box size of the simulation

from  $10\text{-}40\ h^{-1}\text{Mpc}$ . We have also run a  $256^3$  simulation to study the effect of resolution and box-size.

When varying the reionisation history we have chosen a default model which reproduces the measured photoionisation rates at  $z \sim 6$  reasonably well, the ‘512-20-good\_l’ model, where 512 stands for our default number of RAMSES resolution elements in one dimension and 20 for the  $20\ h^{-1}\text{Mpc}$  default comoving size of the simulation box. We have further run simulations where hydrogen is reionised later (model ‘late’) and earlier (model ‘early’) and a model where overlap occurs at the same redshift as in the ‘512-20-good\_l’ model but with a somewhat larger ionising emissivity (and thus photoionisation rate) in the phase immediately past overlap (model ‘good\_h’). In tables 1 and 2 we give the basic parameters of our RAMSES simulations as well as the parameters of equation 3. Fig. 1 shows the redshift evolution of the ionising emissivities used in our simulation suite. Fig. 2 shows the corresponding integrated number of ionising photons per hydrogen atom.

Unfortunately, the temperature calculations as implemented in ATON simulations do not properly account for the radiative transfer effects on the temperature as the radiative transfer is modelled monochromatically and not fully coupled to the hydro simulation. As discussed in detail in Puchwein et al. (2015), (optically thin) simulations with the HM2012 UV background model and an equilibrium chemistry solver agree actually reasonably well with measured temperatures of the IGM. We have therefore assumed the temperatures obtained in the RAMSES simulations for the ATON simulations. In Fig. 3, we compare the evolution of the temperature at mean density as a function of redshift in our RAMSES/ATON simulations without radiative transfer to measured temperatures from Becker et al. (2011) assuming a power law index  $\gamma = 1.5$  for the temperature-density



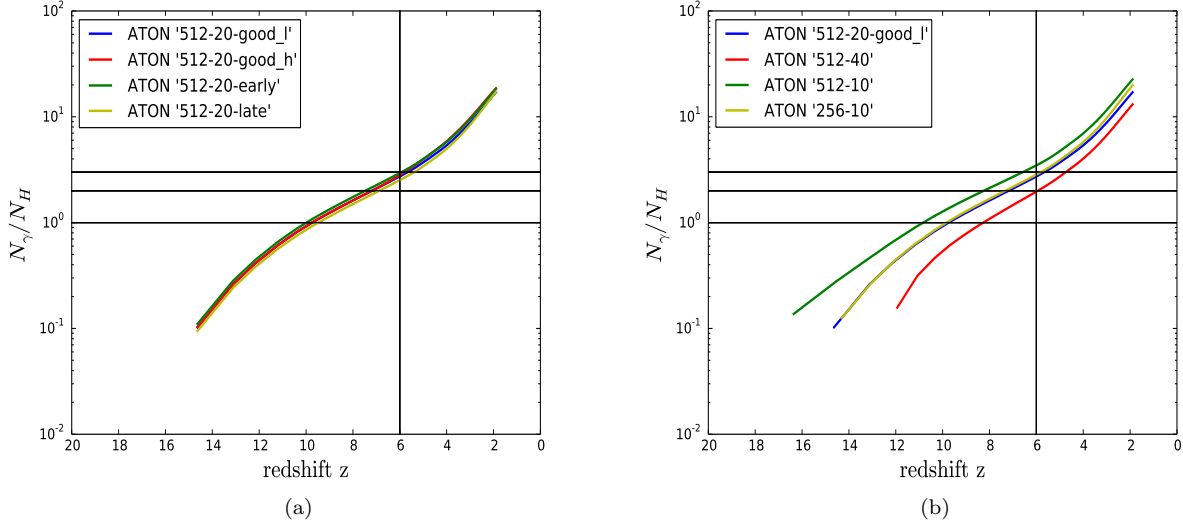


**Figure 2.** (a) The cumulative number of ionising photons emitted per hydrogen atoms as a function of redshift for the ionisation histories in the ATON simulations. (b): same as (a) but for the simulations with different box sizes and resolution as described in the text. The three solid horizontal lines show one, two and three ionising photons emitted per hydrogen atoms at  $z \sim 6$ .

model	512-20-good_l	512-20-good_h	512-20-early	512-20-late
resolution	512 <sup>3</sup>	512 <sup>3</sup>	512 <sup>3</sup>	512 <sup>3</sup>
box size (Mpc/h)	20	20	20	20
minimum halo mass ( $M_{\odot}$ )	$1.2 \times 10^8$	$1.2 \times 10^8$	$1.2 \times 10^8$	$1.2 \times 10^8$
a	1.3	1.3	1.4	1.2
$z_1$	5.8	7	5.8	5.5
$z_2$	5	5	5	5
$\alpha_1$	0.6	0.5	0.6	0.9
$\alpha_2$	1.0	1.1	1.0	0.8

**Table 1.** Basic properties of the simulations for the 512-20 ATON simulations with the different reionisation histories.

relation of the IGM at the relevant densities. The agreement is very reasonable.

### 3 RESULTS

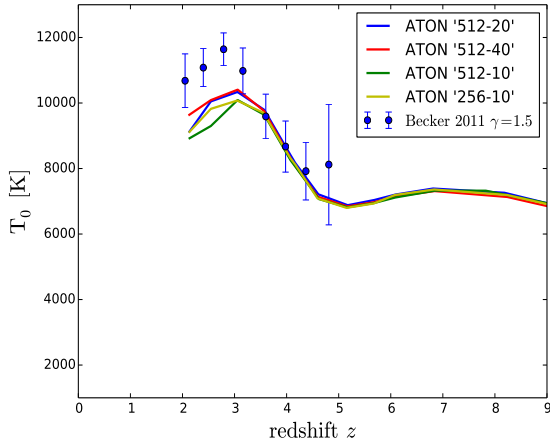
In this section we describe the main results from our ATON simulations. We first focus on the global reionisation history of the different models and compare photoionisation rates and neutral hydrogen fractions to those inferred from Ly $\alpha$  forest data. We then produce mock Ly $\alpha$  forest spectra from our simulations to compare directly to observed properties of the Ly $\alpha$  forest. We finally make some predictions of the UV background fluctuations expected in the later stages of the reionisation from our simulations.

#### 3.1 Reionisation history

##### 3.1.1 Evolution of the neutral hydrogen fraction

Figure 4 shows the evolution of the spatial distribution of the neutral fraction for the ‘512-20-good\_l’ model. Individual HII regions start to appear as early as  $z \sim 16$  and by  $z \sim 10$  there is considerable overlap of HII regions. Contiguous regions of still neutral gas in the post-overlap phase persist to about  $z \sim 7$ . Later on fully neutral gas is expected to be mostly confined to virialized haloes, however the ionising sources in our simulations appear to keep the gas in their host haloes fully ionised. Note that this may be an artefact as the simulation still don’t have the resolution to properly resolve the ISM in these haloes. We also do not include dust and assume that the haloes continuously emit

model	256-10	512-40	512-10
resolution	256 <sup>3</sup>	512 <sup>3</sup>	512 <sup>3</sup>
box size (Mpc/h)	10	40	10
minimum halo mass (M <sub>⊙</sub> )	$1.9 \times 10^8$	$8.9 \times 10^8$	$1.6 \times 10^7$
a	1.36	1.025	1.58
z <sub>1</sub>	6	5.8	6
z <sub>2</sub>	5	5	5
α <sub>1</sub>	0.75	0.5	1.0
α <sub>2</sub>	0.85	1.0	1.0

**Table 2.** Basic properties of the simulations for the simulations with different box sizes and resolution.**Figure 3.** Evolution of the temperature at mean density  $T_0$  in our different RAMSES/ATON simulations. The blue circles with errorbars show observational constraints from Becker et al. (2011) assuming a value of  $\gamma = 1.5$  for the slope of the temperature-density relation. The red squares with errorbars show the recent observational value of Boera et al. (2014), again, assuming a value of  $\gamma = 1.5$  for the slope of the temperature-density relation.

ionising radiation. Note also that we do not have the resolution to properly resolve the majority of mini-haloes with virial temperatures below the atomic cooling threshold. The smallest haloes in our 512-20 simulation have circular velocities of  $v_{\text{circ}} \sim 10.7$  km/s somewhat above the atomic cooling threshold, but even at this resolution the simulations are already significantly incomplete for these haloes (see Appendix A for halo mass functions for our simulation suite). Finally note again that the effect of the reionisation heating is only taken into account by the equilibrium modelling with the HM2012 UV background model in the RAMSES simulations without radiative transfer.

In Fig. 5 we compare the spatial distribution of ionised and neutral regions at  $z \sim 7.1$  of our ATON simulations

(left column) for a range of resolutions and box sizes. The ionisation maps are resolution dependent and in particular the remaining neutral gas in the haloes in already ionised regions is increasing with increasing resolution as the gas in the individual dark matter haloes becomes better resolved and is able to recombine and self-shield due to higher densities. We show the corresponding RAMSES simulations without radiative transfer in the middle column. To make this a fair comparison we have rescaled the photoionisation rate in the RAMSES simulation to be the same as the mean photoionisation rate in the ionised regions in the slice of the ATON simulation shown in the left column.

We have furthermore implemented the self-shielding correction suggested by Rahmati et al. (2013) based on their radiative transfer simulations in the RAMSES simulations without radiative transfer (shown in the right column). In the Rahmati et al. (2013) prescription the self-shielding of the gas is taken into account by a density-dependent photoionisation rate, obtained by an empirical fit to their radiative transfer simulations (Rahmati et al. 2013),

$$\frac{\Gamma_{\text{ss}}}{\Gamma} = 0.98 \times \left[ 1 + \left( \frac{\Delta}{\Delta_{\text{ss}}} \right)^{1.64} \right]^{-2.28} + 0.02 \times \left[ 1 + \frac{\Delta}{\Delta_{\text{ss}}} \right]^{-0.84} \quad (4)$$

where  $\Gamma_{\text{ss}}$  is the value of the photoionisation rate in a cell of the computational box after accounting for self-shielding while  $\Gamma$  is the value of the background photoionisation rate before accounting for self-shielding.  $\Delta_{\text{ss}}$  is the overdensity above which the gas begins to self-shield (see Bolton & Haehnelt 2013),

$$\Delta_{\text{ss}} = 36 \times \Gamma_{12}^{2/3} T_4^{2/15} \left( \frac{\mu}{0.61} \right)^{1/3} \left( \frac{f_e}{1.08} \right)^{-2/3} \left( \frac{1+z}{8} \right)^{-3} \quad (5)$$

where,  $\Delta = \rho/\bar{\rho}$  is the overdensity,  $\Gamma_{12} = \Gamma/10^{-12} \text{s}^{-1}$  is the background photoionisation rate,  $T_4 = T/10^4 \text{K}$ , with  $T$  the temperature of the gas,  $\mu$  is the mean molecular weight

and  $f_e = n_e/n_H$  is the free electron fraction with respect to hydrogen.

We have chosen  $z = 7.1$  for this comparison as there is particular interest in this redshift due to the highest redshift QSO ULAS J1120+0641 at  $z = 7.085$  which may show signs of a red damping wing in its absorption spectra (Mortlock et al. 2011, Bolton et al. 2011, but see Bosman et al. 2015 (in prep)). Note that while there are still substantial contiguous neutral regions extending well beyond the extent of individual haloes in the ATON simulations the volume filling factor of the neutral gas in the optically thin simulations is considerably smaller and is confined to the haloes even when self-shielding with the Rahmati et al. (2013) prescription is taken into account. The self-shielding of dense gas in haloes located in already ionised regions of the ATON simulations is considerably weaker than predicted by the Rahmati et al. (2013) model which does not account for the local ionising sources located in these haloes which are emitting with constant emissivity in our models.

Figure 6 shows the evolution of the spatial distribution of the neutral fraction at three redshifts for the four ‘512-20’ models with the corresponding emissivities reported in Table 1. As expected, increasing/decreasing the emissivities accelerates/delays reionisation. The different models bracket a reasonable range of reionisation redshifts. The differences in the timing of the reionisation process between the different models are further quantified in the upper left panel of Figure 7 that shows the evolution of the mean neutral fraction, while the bottom left panel of the same figure shows the evolution of the volume filling factor for our suite of simulations. As already mentioned our ‘good’ models were chosen such that hydrogen reionisation is mostly completed by  $z = 6 - 6.5$ . At this redshift the still neutral regions cease to hang together and become separate islands and the mean neutral fraction drops rapidly by several orders of magnitudes to a level of  $f_{\text{HI}} \approx 10^{-4}$ , while the volume filling factor of ionised regions rises to  $Q_{\text{HII}} = 1$ . The same happens at somewhat lower/higher redshift in our late/early model.

Figure 8 shows the integrated Thompson optical depth for our simulation suite,

$$\tau(z) = c\sigma_t \int_z^0 n_e(z) \frac{dt}{dz} dz, \quad (6)$$

where  $\sigma_t$  is the Thompson cross section of the electron, and  $n_e(z)$  is the electron density. At low redshift, where the Universe is fully ionised the curves all converge. Our reionisation histories are all somewhat below the mean value of the 2013 Planck+WMAP data results and are in excellent agreement with the Planck 2015 TT+lowP+lensing results. There is little dependence of the Thomson optical depth on resolution as we have adjusted the emissivity to obtain similar reionisation redshifts. The slightly earlier reionisation in the ‘256-10’ model results in a somewhat larger optical depth as expected. Note that we have assumed here that He becomes singly ionised in regions where hydrogen is ionised. Note further that the reionisation history at high redshift (say  $z > 10$ ) is poorly constrained by our comparison to Ly $\alpha$  forest data. There should thus exist models with a different evolution of the ionising emissivity at very high redshift (where we have not modified here the redshift evolution assumed in HM2012) that are equally consistent with

the Ly $\alpha$  forest data and have a different Thomson optical depth.

### 3.1.2 Photoionisation rate and mean free path of ionising photons

The coloured curves in Fig. 9 show the evolution of the space averaged hydrogen photoionisation rate for our ATON simulations. Note that we have excluded not yet ionised regions when calculating the average photoionisation rates. The photoionisation rate is first decreasing as the HII regions expand and the distances from the ionising sources increases and it then increases once overlap is achieved and multiple sources contribute to the local photoionisation rate. By moderately scaling our emissivities with regard to the HM2012 UV background model we succeeded in reproducing the observed photoionisation rates rather well. The only exception is the ‘512-20-late’ model that has photoionisation rates at  $z \geq 5$  somewhat lower than observed. Reionisation appears indeed to happen too late in this model to be consistent with the observed photoionisation rates as we had intended for this model. Tuning the ionising emissivities to reproduce the observed apparent lack of evolution of the photoionisation rate at  $6 > z > 2$  in the other models required a significantly shallower rise of the ionising emissivity compared to the HM2012 model at  $5 > z > 2$  (see Fig. 1) that assumes a rather rapid rise of the ionising emissivity due to QSOs in this redshift range (see Tables 1 and 2 for the coefficients of the power law of equation 3). Note that Muñoz et al. (2014) came to similar conclusions based on their analytic modelling of photoionisation rates. Our ‘good\_l’ and ‘good\_h’ models nicely bracket the inferred photoionisation rate at  $6 > z > 5$  where the photoionisation rate is most difficult to measure and also evolves rather rapidly.

To better understand the evolution of the photoionisation rates it is illustrative to also have a look at the evolution of the mean free path of ionising photons relative to the mean distance between its sources which we show in Fig. 10. In all models the mean free path shown by the solid coloured curves is initially shorter than the mean distance between ionising sources and rises slowly with decreasing redshift until mean free path and mean distance between sources become similar. Soon afterwards the ionised regions fully percolate and the mean free path rises very rapidly. The evolution of the photoionisation rate then scales as the product of ionising emissivity and mean free path,  $\Gamma \propto \epsilon_{\text{ion}} \lambda_{\text{mfp}}$ . The photoionisation rate therefore shows a similar rapid rise when the ionised regions fully percolate. This behaviour of  $\Gamma$  and  $\lambda_{\text{mfp}}$  has already been discussed for the early cosmological radiative transfer simulations by Gnedin (2000). There is good agreement with observations of the mean path as compiled by Worseck et al. (2014), but note that as discussed by Becker & Bolton (2013) at  $z \lesssim 4$  the approximation made here that the mean-free path is small compared to the Hubble radius becomes rather poor. At  $z \lesssim 4$  redshifting of ionising photons between emission and absorption has to be taken into account for a proper comparison of the mean free path predicted by the simulation and that inferred from Ly $\alpha$  forest data.

For reference we also show the mean free path corresponding to the assumed opacity in the HM2012 UV background model. There is a clear trend of increasing mean free

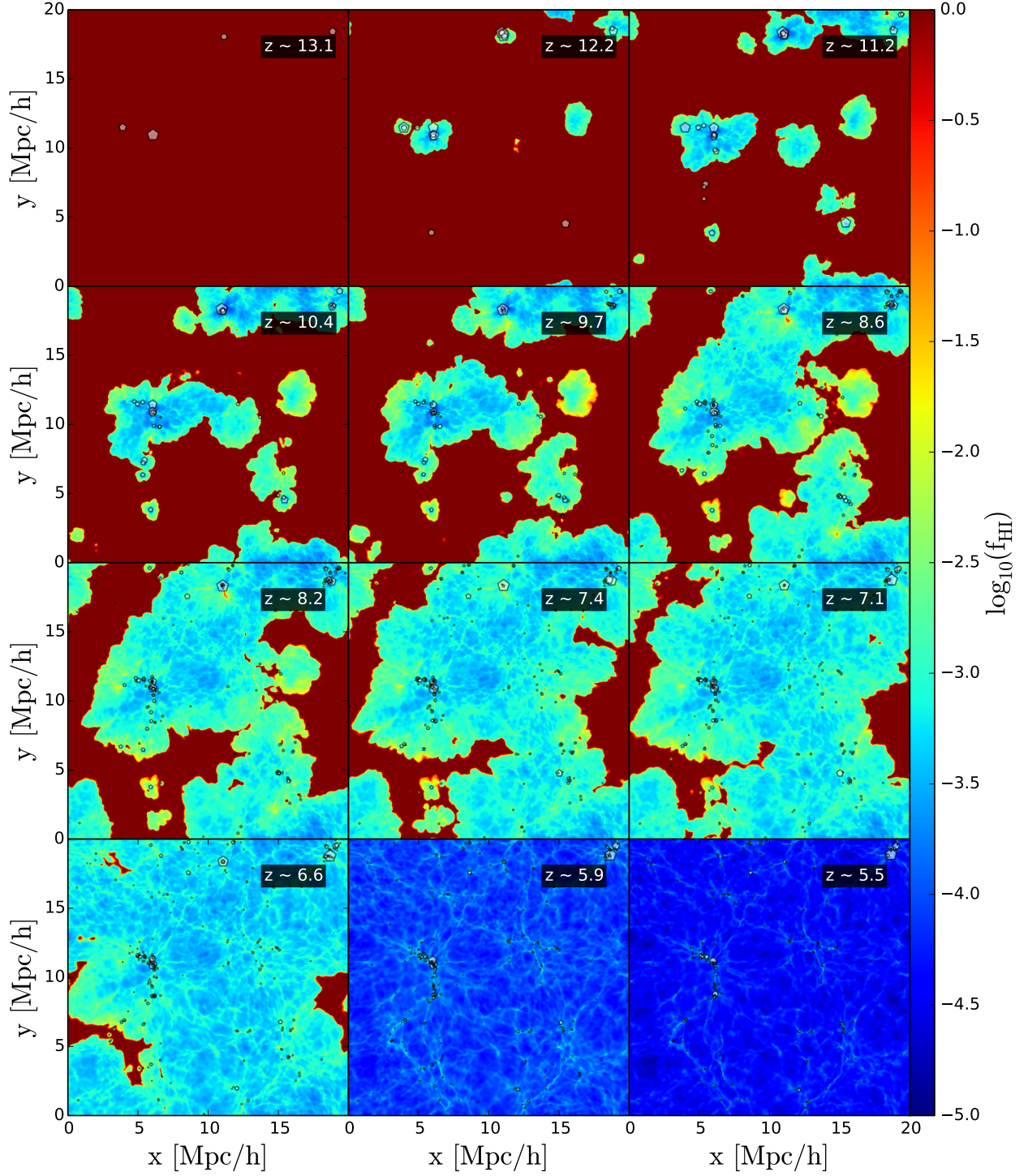


**Figure 4.** Evolution of the spatial distribution of the neutral fraction for the ‘512-20-good.l’ model for a slice of 39.06 comoving kpc thickness in the mid plane of the simulation. The white pentagons indicate the location of the dark matter haloes assumed as ionising sources with the size scaled to the mass of the halo.



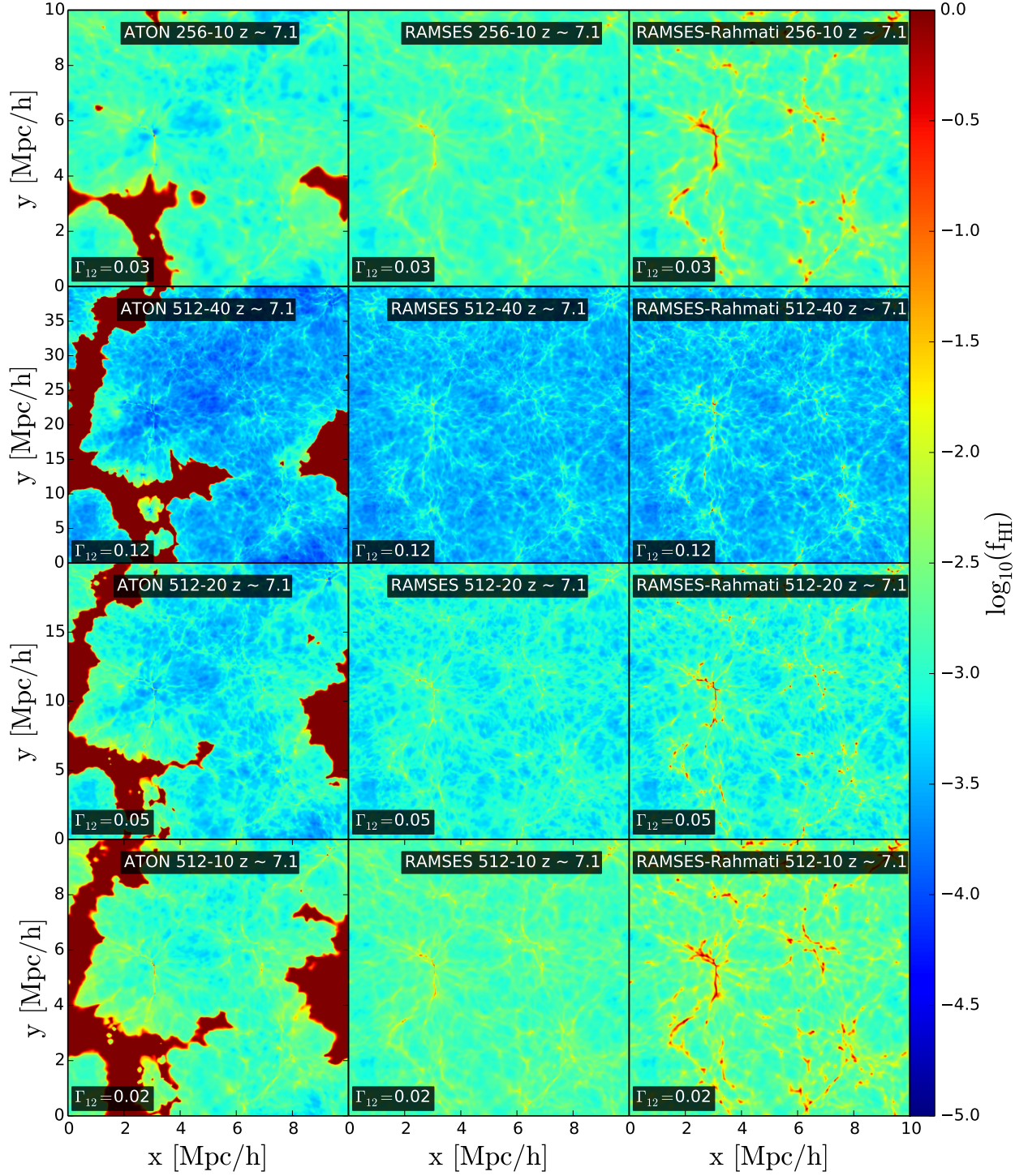


**Figure 5.** Spatial distribution of the neutral fraction at  $z = 7.1$ : First, second, third and fourth rows are for the ‘256-10’ simulation, the ‘512-40’ simulation, the ‘512-20-good\_l’ simulation and ‘512-10’ simulation, respectively. The first column shows the full radiative transfer simulations with ATON. The second column shows the optically thin RAMSES simulations with photoionisation rate rescaled to match that of the corresponding ATON simulation in the first column. The third column shows the RAMSES outputs post-processed with the model/fit of Rahmati et al. (2013) to account for self-shielding to ionising photons. The photoionisation rate in the slices shown is indicated on the plot.

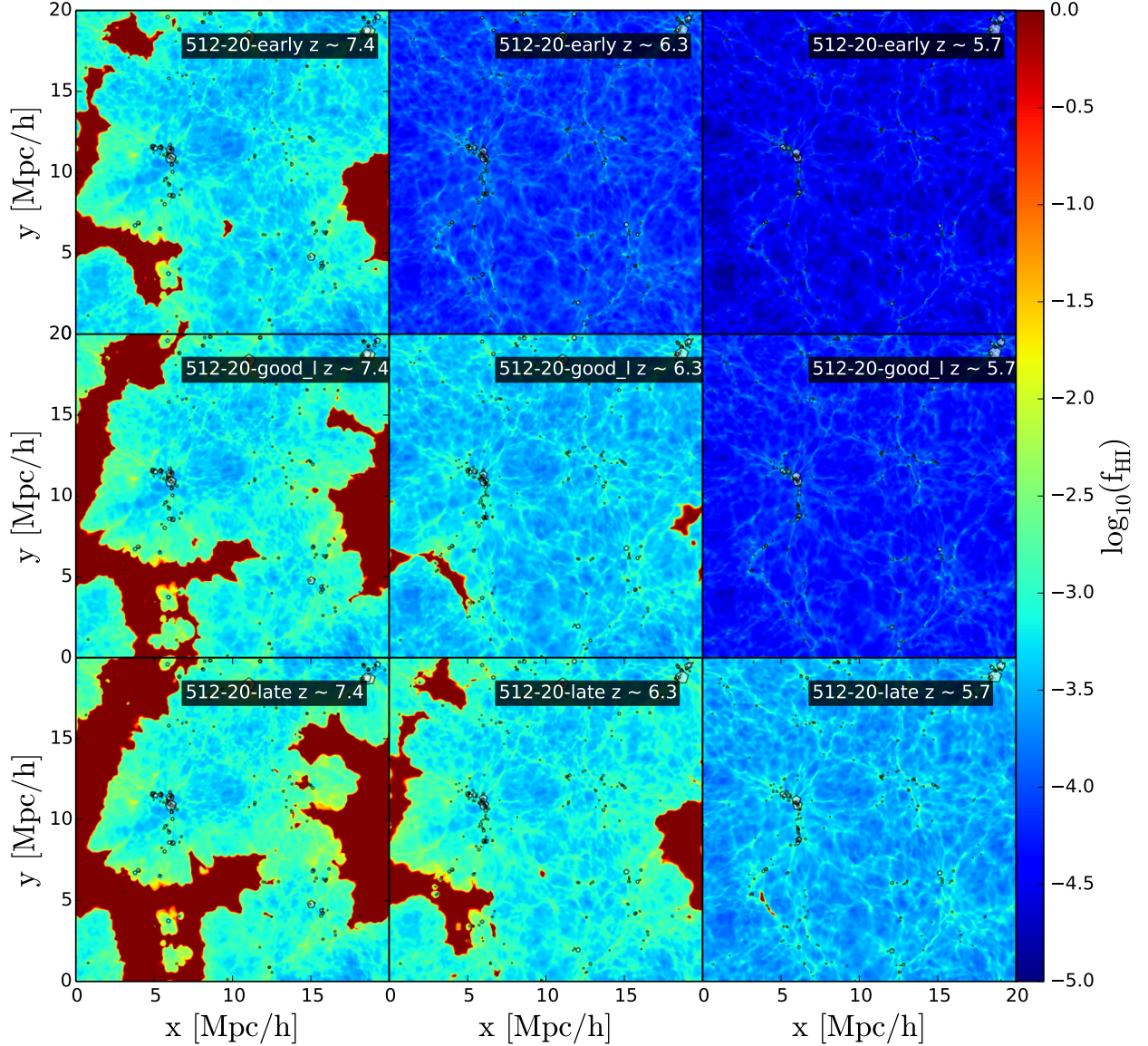


**Figure 6.** The spatial distribution of the neutral fraction at  $z = (7.5, 6.3, 5.7)$  for the different ionisation histories in our ATON simulations. First, second and third rows corresponds to the ‘512-20-early’, ‘512-20-good\_l’ and the ‘512-20-late’ models. The white pentagons indicates the location of the dark matter haloes assumed as ionising sources with the size scaled to the mass of the halo.

path (as well as photoionisation rate) with increasing box size and decreasing resolution. Full details about how the mean free path is measured from the simulations are given in Appendix C.

### 3.2 Spatial UV background fluctuations in the full radiative transfer simulations with ATON

Here we will have a closer look at the spatial fluctuations of the photoionisation rate in our full radiative transfer simu-

lations. In Fig. 11, we show the PDF of the photoionisation rate  $\Gamma_{12}$  in our different ATON simulations for a range of redshifts as well as the value of  $\Gamma_{12}$  of the HM2012 model used in the RAMSES simulations without radiative transfer at those redshifts.

The first thing to note is that, at low redshift, the PDF of the photoionisation rate is strongly peaked and that the spatial fluctuations are rather small. With increasing redshift the distributions broadens considerably and a significant tail towards low values of  $\Gamma$  develops.



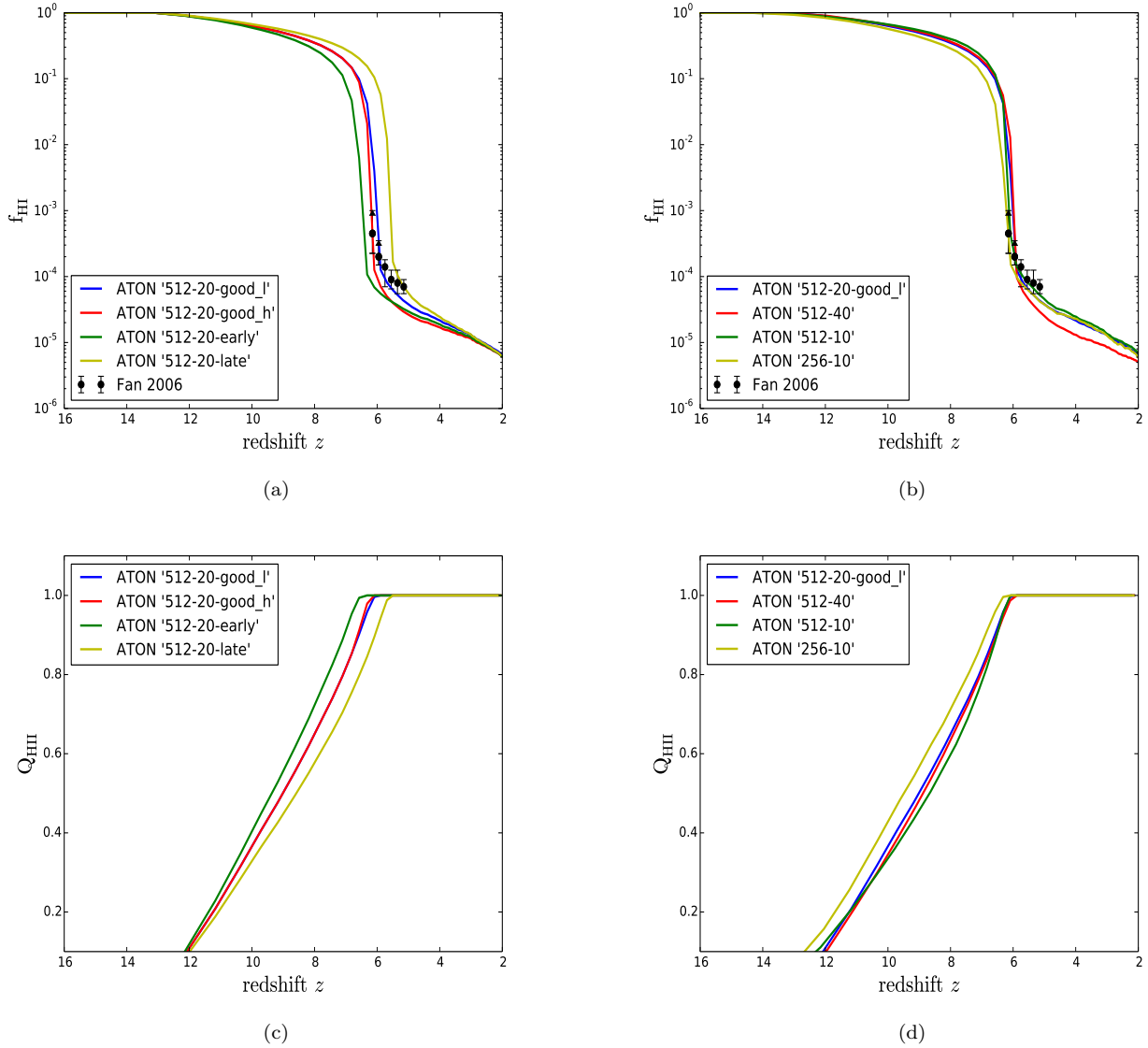


**Figure 7.** (a) Evolution of the mean volume-weighted neutral fraction for the ATON simulations with different reionisation histories, (b) same as (a) for the simulations with different box sizes and resolutions, (c) evolution of the volume filling factor of ionised regions (with an ionisation fraction  $\geq 0.5$ ) for the ATON simulations with different reionisation histories, (d) same as (c) for the simulations with different box sizes and resolutions. The data points are from Fan et al. (2006) and are based on an analytical model for the opacity PDF.

As expected the damping of the spatial fluctuations correlates with the timing of reionisation and (moderate) spatial fluctuations persist for some time after full percolation has occurred.

The trend of increasing mean photoionisation rate with increasing box size and decreasing resolution is again clearly recognisable. Other possible trends in the PDF of  $\Gamma$  with the simulations of different box size and resolution appear to be weak.

### 3.3 Reproducing Lyman- $\alpha$ forest data

#### 3.3.1 Extracting mock Lyman- $\alpha$ forest spectra

We have produced mock absorption spectra from our simulations for comparison with  $\text{Ly}\alpha$  forest data as e.g. described in Theuns et al. 1998. For this we used the gas density, gas temperature, gas velocity and ionisation state of the gas in the simulation boxes and compute Lyman- $\alpha$  absorption spectra along random lines of sight. We did this for both the RAMSES simulations without the radiative transfer and the ATON simulations. Note again that the temperatures of the (optically thin) RAMSES simulation were used throughout as discussed in section 2.4. We have extracted 5000 spectra from each simulation output. For comparison with the ob-

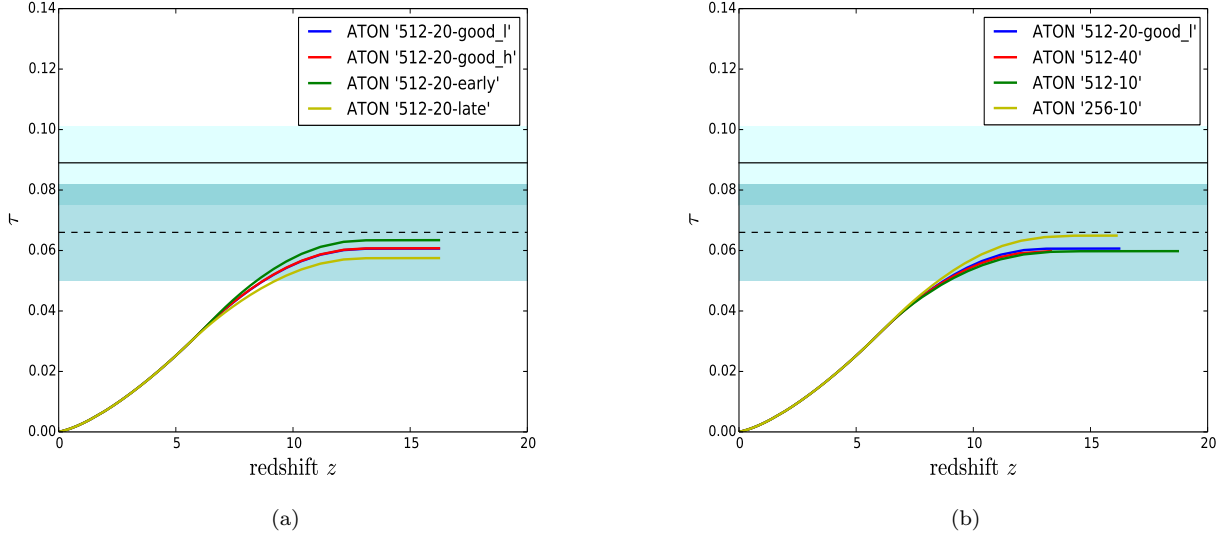


**Figure 8.** (a) The integrated Thompson optical depth for the ATON simulations with the different reionisation histories. (b): Same as (a) for the simulations with different box sizes and resolution. The solid black line with the light blue area represents the 68% confidence limits from the 2013 Planck+WMAP data (see Planck Collaboration et al. 2014). The dashed black line with the shaded dark blue area represents the 68% confidence limits from the Planck 2015 TT+lowP+lensing data release (see Planck Collaboration et al. 2015).

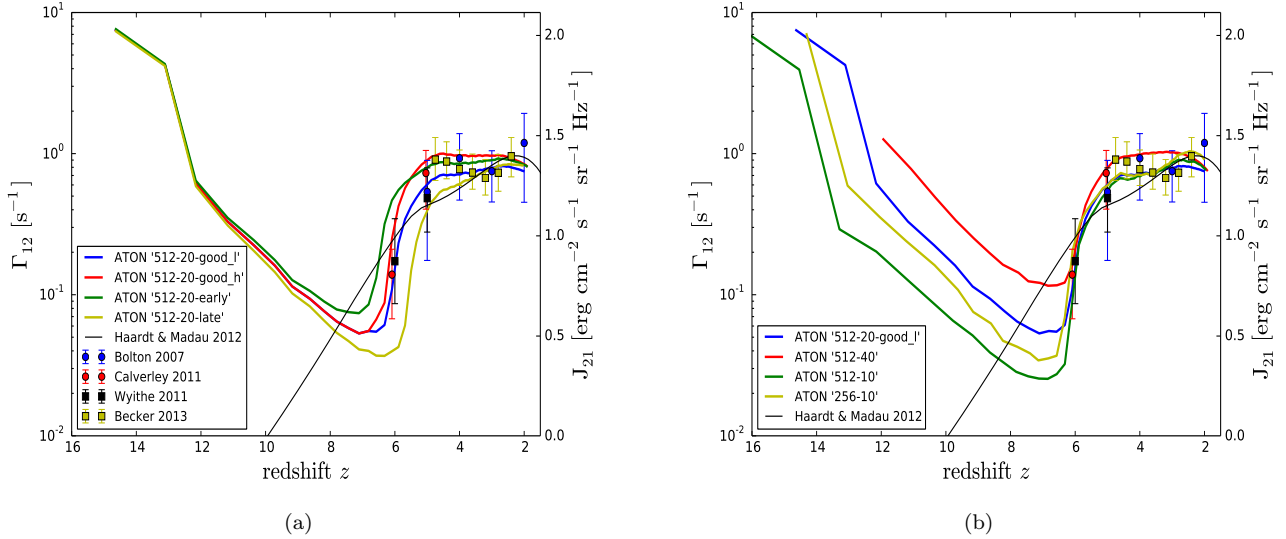


**Figure 9.** (a) Evolution of the hydrogen photoionisation rate for the ATON simulations with different reionisation histories (computed in ionised regions with an ionisation fraction  $\geq 0.5$ ). (b) same as (a) for the simulations with different box sizes and resolutions. The solid black line shows the evolution of the photoionisation rate in the uniform HM2012 UV background model. The observational constraints are from Bolton & Haehnelt (2007), Calverley et al. (2011), Wyithe & Bolton (2011) and Becker & Bolton (2013). Note that the data points have been rescaled (by factors ranging from 0.85 to 1.03) to that inferred for the cosmological parameters and temperature-density relation in our RAMSES simulations with the scaling relation in Bolton et al. (2005) and Bolton & Haehnelt (2007).

served Ly $\alpha$  opacity PDF we concatenated simulated spectra to a length covering a comoving distance of 50 Mpc/h, the length chosen by Becker et al. (2015) for their measurements.

### 3.3.2 Effective optical depth

We expect our simulations to reproduce the properties of the  $2 < z < 4$  Ly $\alpha$  forest data reasonable well as our optically thin 512 $^3$  RAMSES simulations are very similar to P-GADGET3 simulations that some of us have compared extensively to Ly $\alpha$  forest data in the past.

In Fig. 12, we compare the evolution of the effective op-



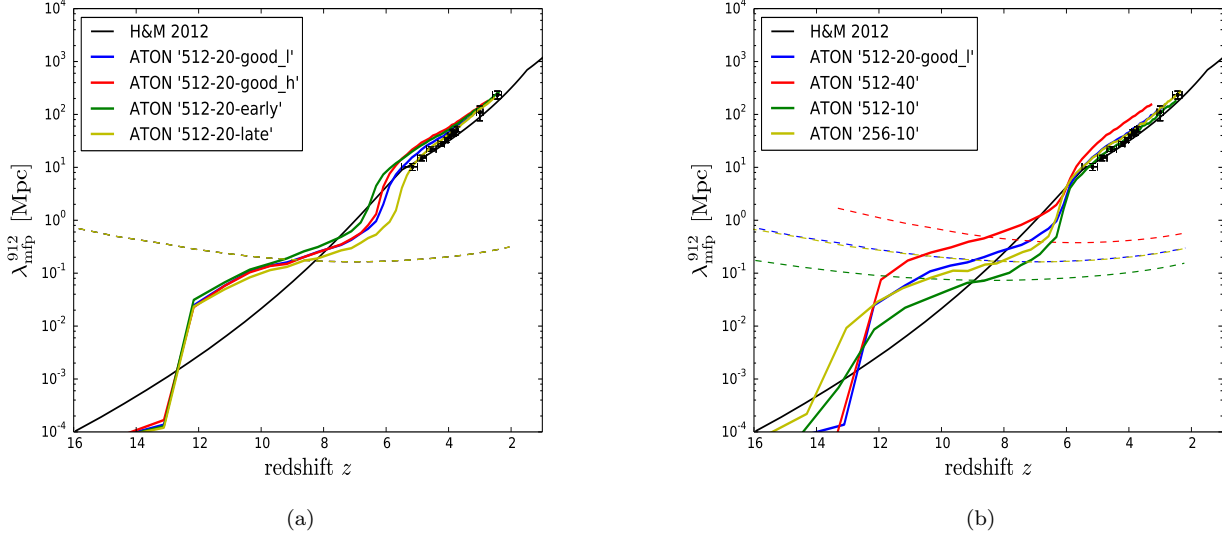


**Figure 10.** (a) Evolution of the space averaged mean free path of Lyman limit (912 Å) photons (in proper Mpc) for the ATON simulations with different reionisation histories (including both ionised and neutral regions). (b) same as (a) for the simulations with different box sizes and resolutions. The dashed curves show the evolution of the mean distance between ionising sources in the different ATON simulations. The black squares with errorbars show observational constraints from O’Meara et al. (2013) at  $z = 2.44$ , Fumagalli et al. (2013) at  $z = 3.00$ , Prochaska et al. (2009) at  $z = 3.73$ , and Worseck et al. (2014) at  $z = 4.56$  as compiled by Worseck et al. (2014). The black solid line shows the evolution in the HM2012 model.

tical depth  $\tau_{\text{eff}}(z)$  calculated from 5000 spectra for each of our simulations with a range of measurements of the effective optical depth as described in the figure caption. Both ‘good’ models reproduce the rapid rise of the observed optical depth at  $z \sim 5.5$  very well, while in the ‘early’ and ‘late’ models reionisation is completed indeed somewhat early and late, respectively. The effective optical depth of our ‘good.h’ model goes thereby right through the middle of the observed measurements of  $\tau_{\text{eff}}$  which however show a large scatter. The effective optical depth of the ‘good.l’ model on the other hand goes through the upper envelope of observed measurements at  $5 < z < 6$  as expected from our comparison of simulated photoionisation rates and those inferred from Ly $\alpha$  forest data in section 3.1.2. Note that our full radiative transfer simulations with the rescaled emissivities compared to the HM2012 reproduce the observed  $\tau_{\text{eff}}$  significantly better than the optically thin RAMSES simulations with the HM2012 model. The latter somewhat overproduces the observed  $\tau_{\text{eff}}$  at  $4 < z < 6$  and shows a somewhat slower evolution with redshift than observed. This confirms similar findings by Puchwein et al. (2015) based on optically thin P-GADGET3 simulations. The ionising emissivities in the HM2012 UV background model at  $5 < z < 6$  appear to be somewhat lower than necessary to reproduce the Ly $\alpha$  forest data. Judging from Fig. 1 the rather rapid increase of the ionising emissivity at  $3 < z < 6$  due to QSOs appears at fault here. An increased contribution from faint AGN at  $z > 4$  (e.g. Giallongo et al. 2015) could provide a redshift evolution in better agreement with the opacity data.

### 3.3.3 The incidence of Lyman limit systems

Another important test of the (residual) neutral hydrogen distribution regulating the Ly $\alpha$  opacity are Lyman Limit Systems in QSO absorption spectra. For this purpose, we calculated the evolution of the incidence rate of absorbers  $dN/dX$  where  $X$  is the usual absorption distance,

$$X = \int_0^z \frac{H_0}{H(z')} (1+z')^2 dz'. \quad (7)$$

and  $H(z)$  is the Hubble constant at redshift  $z$  (Bahcall & Peebles 1969).

In practice we search in our mock spectra for all optically thick pixels ( $\tau > 3$ ). We compute then the column density of each connected absorber defined in that way and select those with  $N_{\text{HI}} \geq 10^{17} \text{ cm}^{-2}$  as Lyman Limit Systems (LLSs). We thereby exclude regions not yet ionised where the occurrence of LLSs is poorly defined.

In Fig. 13 we compare the evolution of  $dN/dX$  for all our simulations to the observed incidence rate from a cumulation of Ly $\alpha$  forest data as described in the figure caption. The solid curves show the results for the ATON simulations while the dashed and dotted curves are respectively for the optically thin simulations without and with the Rahmati et al. (2013) self-shielding correction (see also Kohler & Gnedin 2007 and McQuinn et al. 2011).

Overall the simulations reproduce the increase of the incidence rate of LLSs with increasing redshift very well, but underpredict the observed incidence rate by about a factor 1.5-2 for the ATON simulations as well as for the RAMSES simulations without radiative transfer. This is similar to what has been found by other studies in the literature. In optically thin simulations without (supernovae) feedback

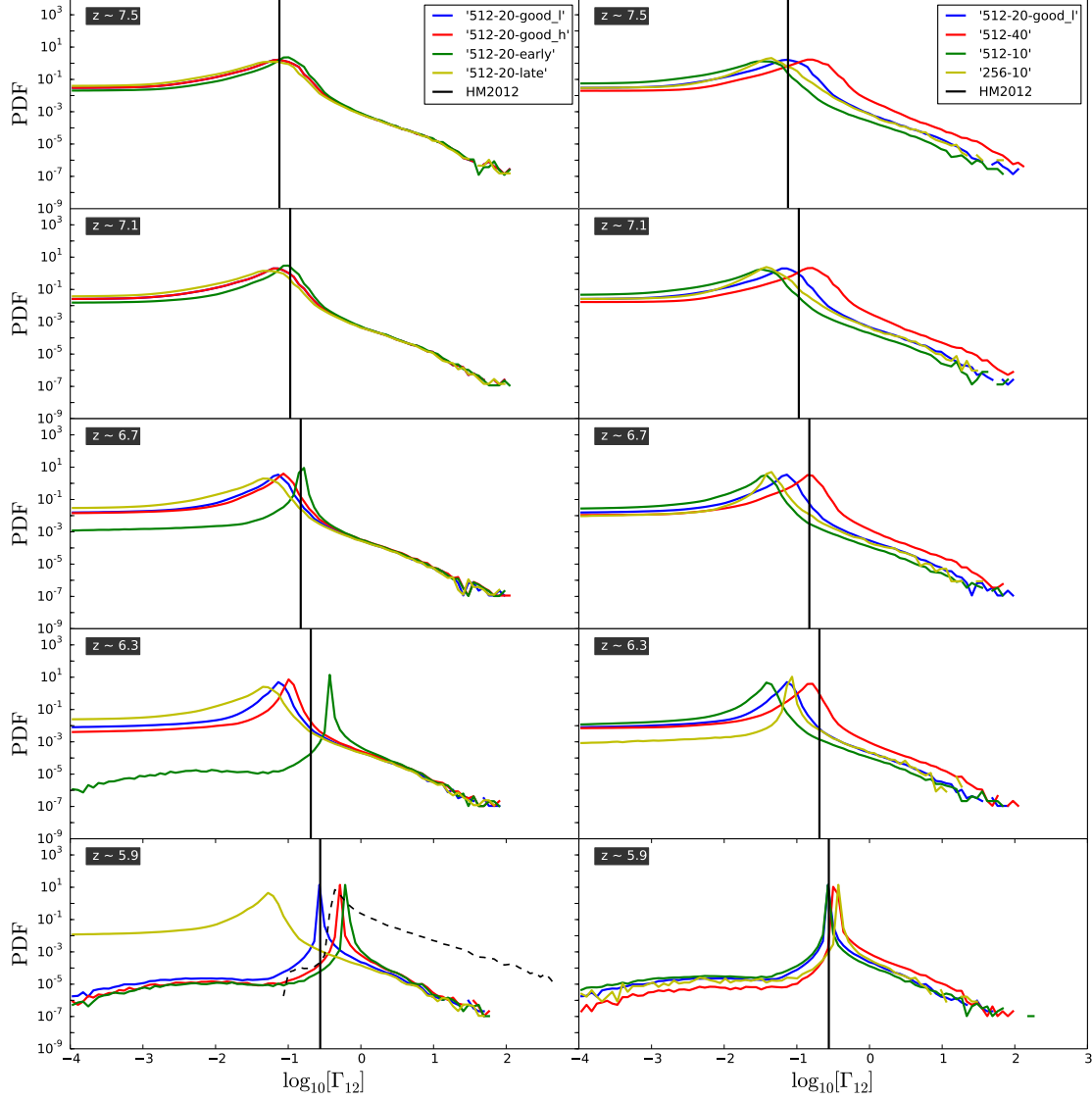


**Figure 11.** Probability distribution function (PDF) of the photoionisation rate ( $dP/d\log_{10}\Gamma_{12}$ ) at five different redshifts in our ATON simulations with different reionisation histories (left column) and for the simulations with different box sizes and resolutions (right column). The solid black vertical lines show the values of  $\Gamma_{12}$  in our RAMSES simulations without radiative transfer based on the HM2012 UV background model (their Table 3) at the same redshifts. The dashed black curve in the bottom left panel shows the PDF of our ‘bright source’ model discussed in section 3.3.4 and Appendix D.

the neutral hydrogen distribution in galactic haloes is generally found to be too spatially concentrated to reproduce the observed LLS incidence rate (Schaye et al. 2010; Altay et al. 2013; Bird et al. 2014).

Fumagalli et al. (2011) used high-resolution zoom simulations to demonstrate that local stellar radiation further reduces the abundance of high column density absorbers. Similar conclusions have been reached by Rahmati et al.

(2013) who found that radiative transfer simulations with local stellar sources underpredict the rates of incidence of absorbers with column densities  $10^{19} < N_{HI} < 10^{21}\text{cm}^{-2}$  by factors of a few.

Simulations with the same resolution but different box size (i.e. the 512-20-good and the 256-10 models) show very similar evolution. There is, however, a clear increase of the incidence rate of LLSs with increasing resolution at  $z > 2.5$

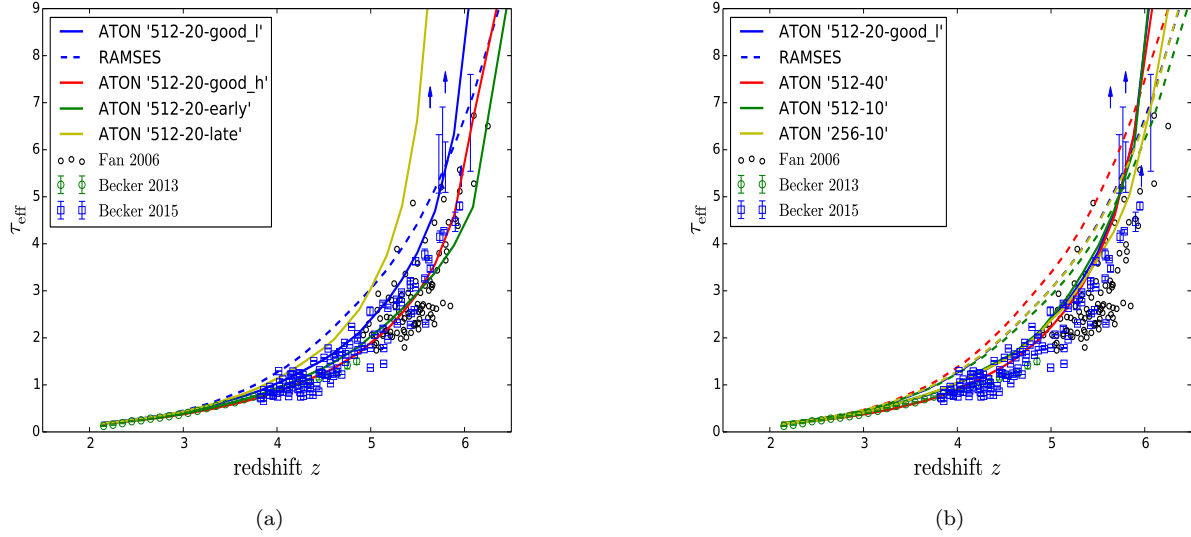


**Figure 12.** (a) The coloured solid curves show the evolution of the effective Ly $\alpha$  optical depth  $\tau_{\text{eff}}(z)$  for the ATON simulations with the different ionisation histories, (b) same as (a) for the simulations with different box sizes and resolutions. The dashed curves correspond to the evolution of  $\tau_{\text{eff}}(z)$  for the RAMSES simulations without radiative transfer. The black data points show the observed  $\tau_{\text{eff}}$  for the QSOs presented in Fan et al. 2006, the green data points show observational constraints from Becker et al. (2013) and the blue data points show the observed  $\tau_{\text{eff}}$  for the QSOs presented in Becker et al. (2015).

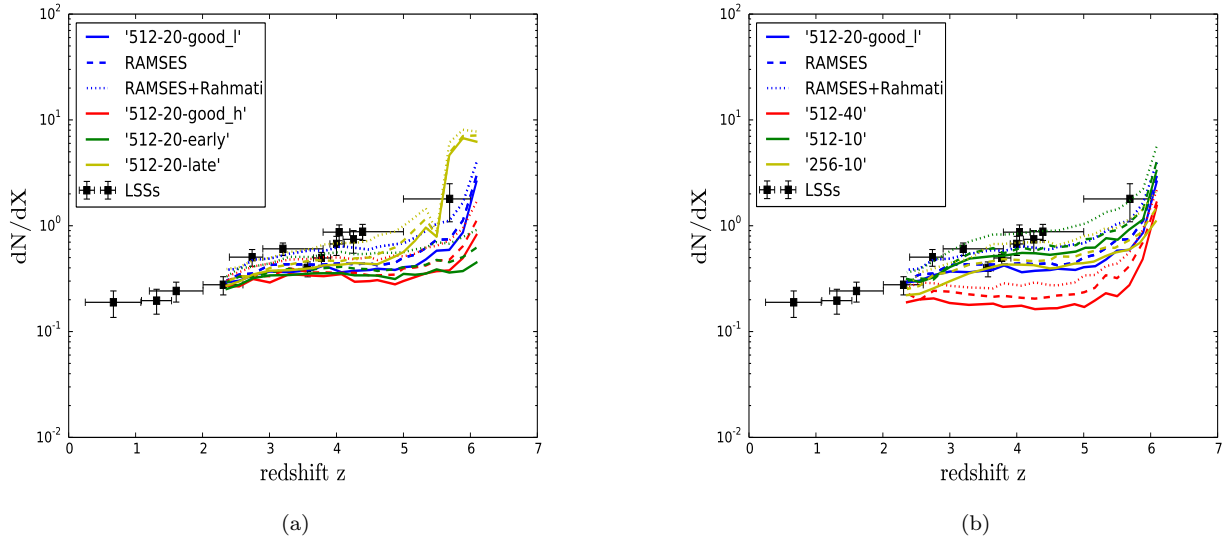


**Figure 13.** (a) The coloured solid curves show the evolution of the incidence rate  $dN/dX$  of LLSs for the ATON simulations with the different ionisation histories, (b) same as (a) for the simulations with different box sizes and resolutions. The dashed curves are for the RAMSES simulations and the dotted curves are for the RAMSES simulations post-processed with the self-shielding correction of Rahmati et al. (2013). For the RAMSES and RAMSES with self-shielding correction simulations, the neutral fraction of the gas has been rescaled to be consistent with the mean  $\Gamma$  value of the corresponding ATON simulations. The black data points with error bars show the measured incidence rate of LLSs (from Songaila & Cowie 2010 and Fumagalli et al. 2013).

and our highest resolution 512-10 model starts to match the data reasonably well. Part of the discrepancy between observed and simulated LLS incidence rate is therefore clearly due to insufficient resolution and not the lack of stellar feedback in our simulations. Note that our RAMSES simulation with the Rahmati self-shielding prescription tend to give

slightly larger LLS incidence rates than our full radiative transfer simulations with ATON where ionising sources are located within the LLS.

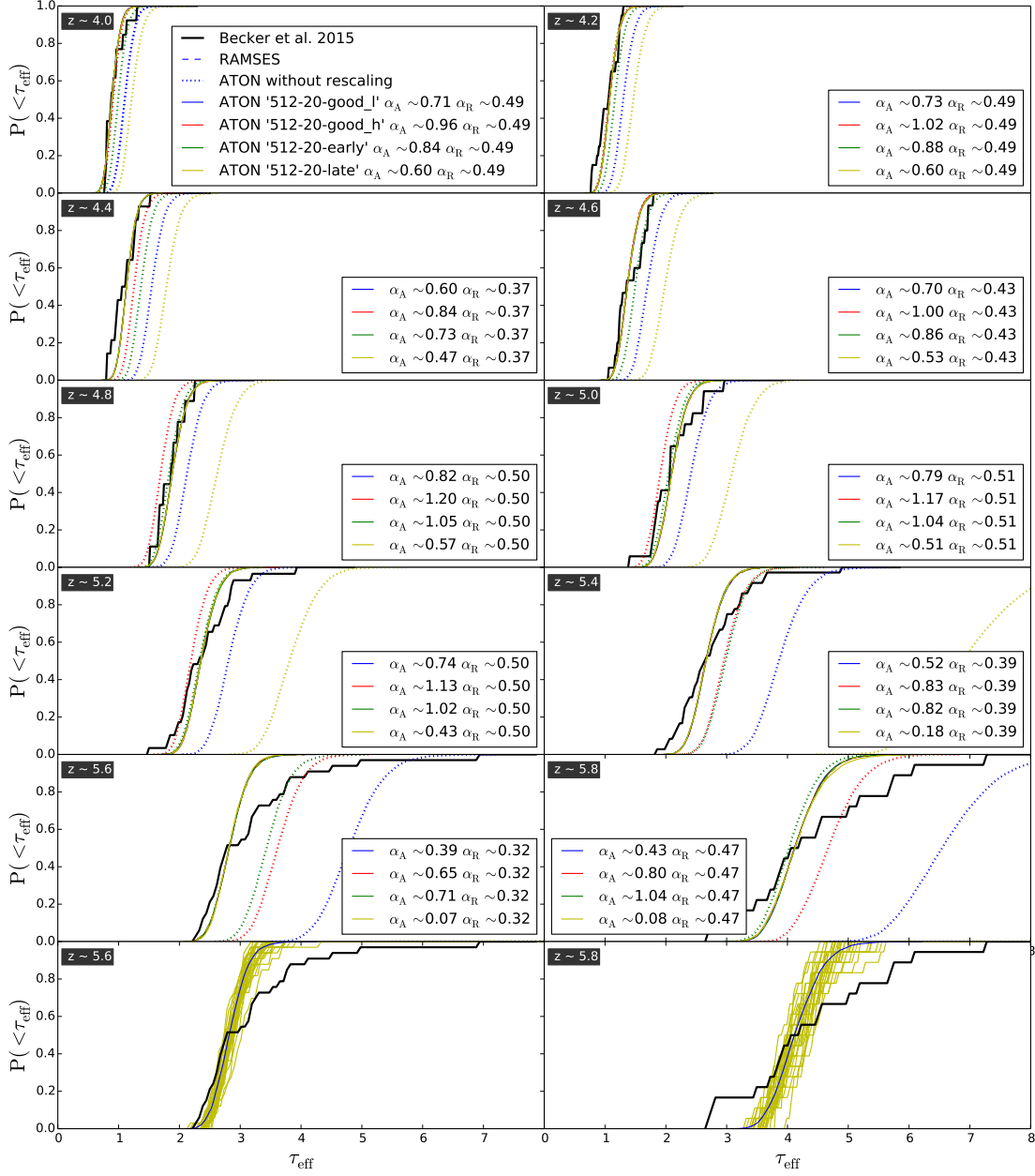


**Figure 14.** The coloured solid curves show the cumulative PDF of the effective optical depth  $\tau_{\text{eff}}$  for our ATON simulations at ten different redshifts as indicated on the plot. The effective optical depths are computed for chunks of 50 comoving Mpc/h as in the observed sample. The dashed curves show the corresponding distributions for the RAMSES simulations without radiative transfer. The  $\alpha_A$  and  $\alpha_R$  values in the labels of the different panels are the factors by which we have rescaled the optical depth of the ATON and RAMSES simulations to match the measurements of Becker et al. (2015) shown by the solid black curves at  $P(\tau_{\text{eff}}) = 0.5$ . The dotted curves show the corresponding distributions of the ATON simulations before the rescaling. The two bottom panels show 30 individual realisations (solid yellow curves) of the cumulative flux PDF for the two highest redshift bins for samples of simulated spectra from the 512-20-good.l ATON simulation with total path length equal to that of the observed sample.

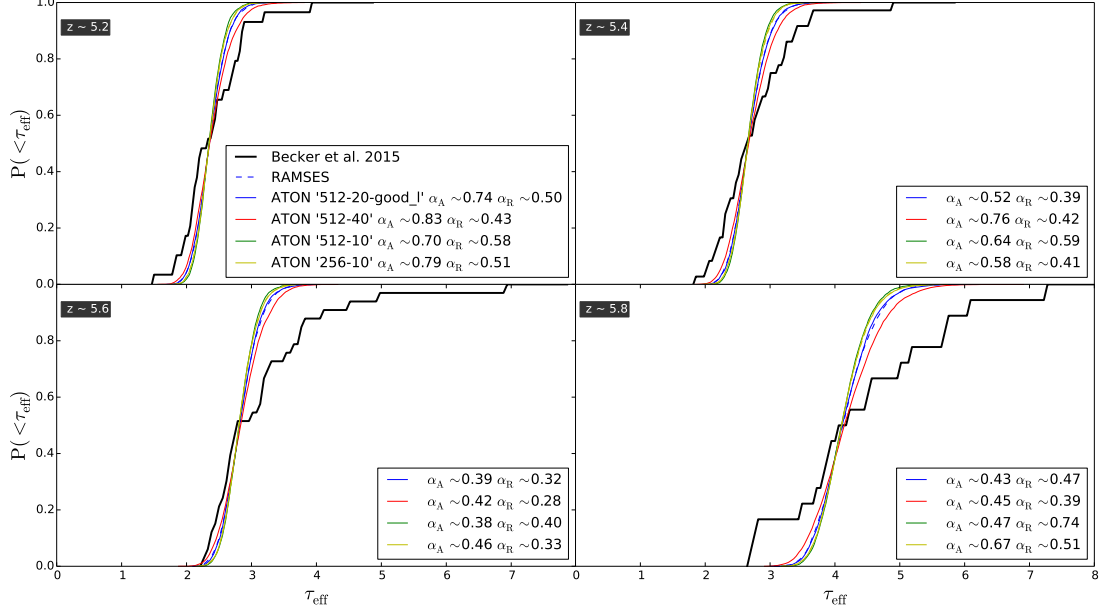


**Figure 15.** Same as figure 14 for the four highest redshift bins for simulation of different box size and resolution.

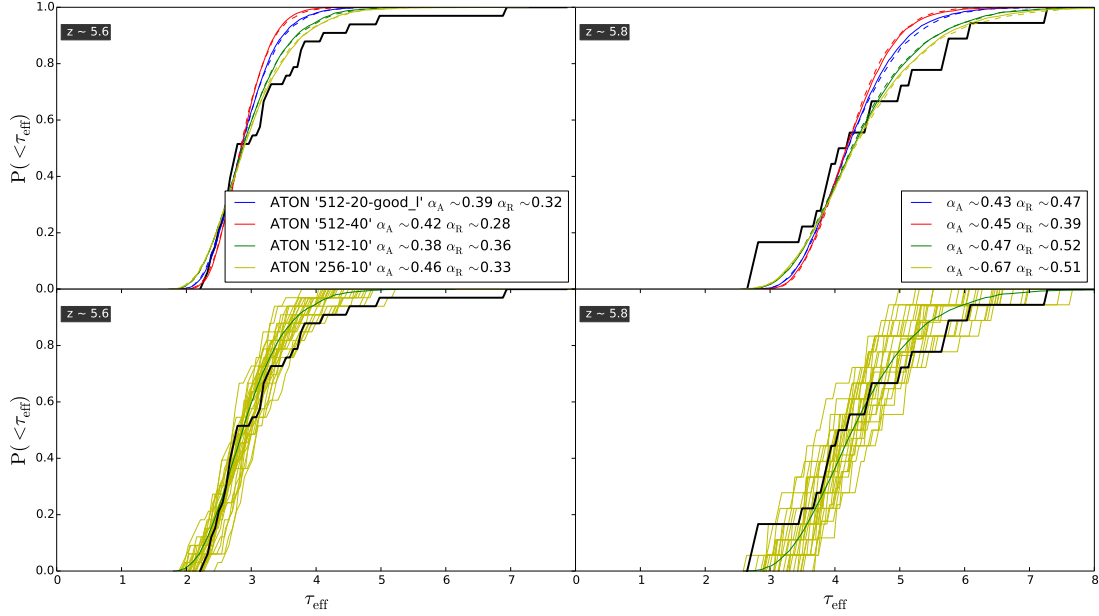


**Figure 16.** Upper panel : the coloured solid curves show the cumulative PDF of the effective optical depth  $\tau_{\text{eff}}$  for our ATON simulations for the two highest redshifts as indicated on the plot. The effective optical depth is now computed for chunks of a length corresponding to the box size in the different simulations instead of chunks of length 50 Mpc/h as before. The two bottom panels show 30 individual realisations (solid yellow curves) of the cumulative flux PDF for the two highest redshift bins for samples of simulated spectra from the '512-10' ATON simulation with total path length equal to that of the observed sample. The effective optical depth is again computed for chunks equal to the box size of the simulation, 10 Mpc/h in that particular case.

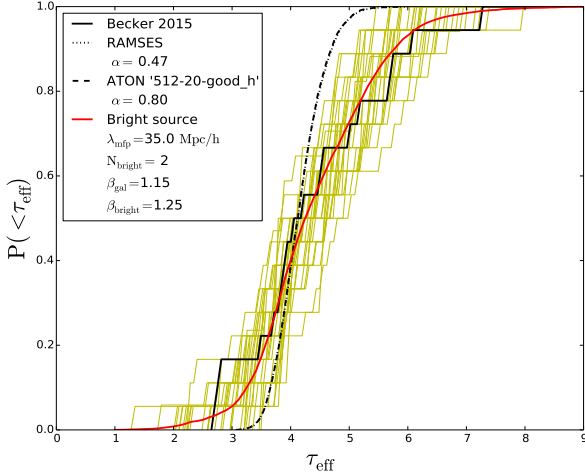


**Figure 17.** The red solid curve shows the cumulative effective optical depth PDF for a “bright source model” with two bright ionising sources in a periodically replicated volume of  $(100\text{Mpc/h})^3$  contributing significantly to the ionising UV background at redshift  $z \sim 5.8$ . The solid yellow curves show 30 individual realisations of the cumulative flux PDF for samples of simulated spectra with photoionisation rates of the toy model with total path length equal to that of the observed sample. The assumed contribution from rare bright sources is added to that in our 512-20-good.l ATON simulation such that the mean photoionisation rate is equal to that in the corresponding good.h model. The photoionisation rates are then scaled by a global factor 0.87 to match the observed PDF as measured by Becker et al. (2015). An average mean free path of  $\sim 35$  comoving Mpc/h as in our 512-20-good.h ATON model is assumed for the attenuation of the bright sources. The black dotted and dashed curves show the PDF of the 512-20-good.h ATON simulation and the PDF of our corresponding optically thin RAMSES simulation with optical depths rescaled to match the observed PDF at  $P(<\tau_{\text{eff}}) = 0.5$ . For more details see text and appendix D. The black solid curve shows the data from Becker et al. (2015).

### 3.3.4 The cumulative Ly $\alpha$ opacity PDF

Recently, Becker et al. (2015) have presented accurate measurements of the PDF of the Ly $\alpha$  effective optical depth obtained from chunks of spectra of 50 comoving Mpc/h at  $4 < z < 6$  based on a large sample of high-quality high-redshift QSO absorption spectra. Based on a comparison with P-GADGET3 simulations without radiative transfer similar to our RAMSES simulations Becker et al. (2015) argued that at  $z > 5$  the Ly $\alpha$  opacity PDF deviates increasingly from that expected for a spatially homogeneous UV background and attributed the increasing deviation at the high opacity end to the spatial UV fluctuations expected to persist for some time during the post-overlap phase of hydrogen reionisation. As we have discussed in section 3.2 our full radiative transfer simulations with ATON show such spatial fluctuations, albeit at a rather moderate level.

In Fig. 14 and 15 we compare the cumulative Ly $\alpha$  opacity PDF at  $4 < z < 6$  for our ATON and RAMSES simulation without radiative transfer with the measurements of Becker et al. (2015). As discussed in section 3.3.2 our ATON simulations for the ‘good.h’ model, shown here as the red

dotted curves, reproduce the mean effective optical depth best. At high redshift the observed effective optical depth at a given redshift shows, however, clearly a much larger scatter than in our simulations. The discrepancy is similar to that found by Becker et al. (2015), for their optically thin simulations.

To investigate this further we adjust the optical depth of our simulations by a constant factor such that the mean effective optical depth of the simulated spectra is equal to  $\tau_{\text{eff}}$  of the observed distribution at  $P(\tau_{\text{eff}}) = 0.5$ . The correction factor  $\alpha$  by which the optical depth is multiplied is indicated for each simulation on the plots. Let us now again have a look at Fig. 14 where we compare the different reionisation histories. At  $z < 4.8$  the Ly $\alpha$  opacity PDF from the ATON and optically thin RAMSES simulations are almost identical after rescaling. They also agree very well with the observed PDF, very similar to what was found by Becker et al. (2015) based on their P-GADGET3 simulations. At  $z \sim 5$  and  $z \sim 5.2$  the PDF of the simulated spectra begins to exhibit a somewhat steeper slope than the observed PDF. At  $z > 5.4$  the discrepancy increases and especially in the two highest redshift bins observed and simulated PDF of the effective optical depth are strikingly different.

The observed sample is still rather small. In order to get a feel for the expected sample variations the two bottom panels of Fig. 14 show, for the two highest redshift bins, the observed Ly $\alpha$  opacity PDF with 30 individual realisations for samples of simulated spectra of the ‘520-20-good.h’ model with total path length equal to that of the observed sample. The scatter is substantial, but the discrepancy between observed and simulated PDF is clearly much larger than can be explained with sample to sample variations.

In Fig. 15, we show the Ly $\alpha$  opacity PDF for simulations where we have varied box size and resolution. The differences are moderate. As expected increasing the box size somewhat increases the width of the distribution, but not nearly enough to attribute the discrepancy with the observed PDF to an insufficient box size of our simulations.

That the PDF of the effective optical depth of our ATON and RAMSES simulations are rather similar means that the spatial UV fluctuations in our full radiative simulations are not sufficient to explain the observed rather wide distribution of optical depth at  $5 < z < 6$ . Becker et al. (2015) modelled the expected UV fluctuations in the post-overlap phase for ionising emission from (faint) galaxies. Combining a simple model for the attenuation of ionising photons for plausible assumptions for the mean free path with their optically thin simulations they came to similar conclusions.

Becker et al. (2015) therefore proposed that the increasing tail of large optical depth in their data could be due to large spatial fluctuations of the mean free path of ionising photons expected in the post-overlap phase of reionisation (Furlanetto & Oh (2005), Mesinger & Furlanetto 2009).

To shed further light on this in Fig. 16, we look at the influence of the chunk size used to compute the effective optical depth. We use our simulations of different box sizes for this and set the chunk size equal to the size of the simulation box. Reducing the length of the spectrum used to compute the effective optical depth increases the scatter in  $\tau_{\text{eff}}$  and thus the width of the PDF as expected. Interestingly for a chunk/simulation box size of 10 Mpc/h the optical depth

PDF matches the observed PDF (calculated with a chunk size corresponding to 50 Mpc/h) to within the expected sample variation. Our simulations appear to reproduce the observed range of observed optical depth at a given redshift, but the coherence length of the optical depth appears to be much shorter than observed so that averaging reduces the width of the PDF.

Density fluctuations on these rather large scales are very small. However, as we will show below large scale spatial UV fluctuations that extend over 50 Mpc/h scales or more could explain this large coherence length. As we and Becker et al. (2015) have shown, such fluctuations are, however, at odds with a UV background at  $5 < z < 6$  dominated by the large number of faint galaxies widely believed to be responsible for reionisation. Leaving this point aside here for the moment (we will come back to this in the next section) we explore here a (toy) model (see also Appendix D), where the galaxies driving reionisation contribute only a fraction of the UV background at  $5 < z < 6$ , while the remainder is contributed by much rarer sources (faint AGN or perhaps very bright galaxies).

Figure 17 shows the resulting effective optical depth PDF for a model with two bright sources in a (periodically reproduced) cube with side-length 100 Mpc/h. We have used the photoionisation rates in our ‘512-20-good.1’ model and have added the UV emission from the rare bright sources such as to reproduce the mean  $\Gamma$  of the 512-20-good.h ATON model which is the closest to the observations. The resulting large scale fluctuations of the ionising flux significantly widen the optical depth PDF. As Figure 17 shows this particular set of parameters reproduces the observed PDF at  $z = 5.8$  very well.

The large scale fluctuations of the ionising flux due to the rare sources in this model were calculated with the simple attenuation model first introduced by Bolton et al. (2006) and used by Becker et al. (2015) (but for a much higher space density than considered here). For details and limitations of this toy model we refer the reader once more to Appendix D. When choosing the parameters of the model we found that the optical depth PDF depends very sensitively on the space density of sources, mean free path of ionising sources and fraction of the UV background contributed by rare sources and there will certainly be other parameter choices that will also reproduce the data. We should thus emphasise here that our toy model should just be seen as proof of concept. We will leave a more detailed exploration of the effect of spatial UV fluctuations due to rare bright sources on the effective optical depth PDF to a future paper.

### 3.4 Implications for the role of bright galaxies and (faint) AGN for the origin and evolution of the ionising emissivity at high redshift

As discussed in detail in the previous sections with our ATON simulations we have got good agreement with the current observational constraints from Ly $\alpha$  forest data in the redshift range  $2 < z < 6$ . With a moderate adjustment of the evolution of the ionising emissivity compared to HM2012 we have been able to reproduce the observed evolution of the mean neutral fraction, mean photoionisation

rate, averaged mean free path, mean Ly $\alpha$  opacity and the incidence rate of LLSs.

Similar to results from optically thin simulations we failed, however, with our radiative transfer simulation to reproduce the broad PDF of the optical depth at  $5 < z < 6$  when measured for chunks of 50 Mpc/h as in Becker et al. (2015). We have thereby confirmed the result of Becker et al. (2015) that the corresponding optical depth fluctuations on these large scales are much larger than can be plausibly explained as being due to density fluctuations. Judging from the large differences in the visual appearance of individual QSO spectra, the implied large coherence length of order unity optical depth fluctuations appears to be even larger than 50 Mpc/h. The very extended Gunn-Peterson trough of high Ly $\alpha$  optical depth in ULAS J0148+0600 at  $z \geq 5.5$  is particularly striking in this regard.

Addressing this properly will require much larger simulated regions at similar resolution(s) than we have employed here and will be a formidable computational task. As we have demonstrated with our toy model in the last section a significant contribution to the integrated ionising UV background from bright sources with space densities of order  $10^{-6}(\text{Mpc/h})^{-3}$  appears to be required.

While most of the literature including HM2012 have assumed that the contribution of QSOs drops rapidly at  $z > 4$ , some authors have argued that there may be a significant contribution by AGN to the ionising UV background at  $z > 4$  (see Giallongo et al. 2015 for a recent discussion). As discussed by Haardt & Salvaterra (2015) a contribution of (faint) AGN at  $z > 4$  is consistent with the soft X-ray background, but sources with softer spectra would have to be responsible for driving hydrogen reionisation in order not to exceed measurements of the soft X-ray background. In light of the need for spatial fluctuations of the ionising UV background on scales  $\gtrsim 50$  Mpc/h at  $5 < z < 6$  it appears therefore prudent to also consider the possibility of efficient escape of ionising photons from stars in rare very bright (possibly star bursting) galaxies at  $z > 5$ . These galaxies would, however, have to have unusually hard ionising spectra and large (of order unity) escape fractions to provide the required ionising emissivity. Interestingly the recent discovery of strong CIV emission in high-redshift galaxies by Stark et al. (2015) may point in this direction. In either case the current widely accepted assumption that the ionising UV background at  $z > 5$  is dominated by faint sub- $L^*$  galaxies may need revision.

## 4 CONCLUSIONS AND OUTLOOK

We have calibrated here full cosmological radiative transfer simulations performed with ATON/RAMSES with Ly $\alpha$  forest data and compared them with optically thin RAMSES simulations.

Our main results are as follows.

- Once the amplitude of ionising emissivities in the HM2012 UV background model is rescaled to take into account (the resolution dependent) recombination in the haloes of ionising sources, we were able to obtain reionisation histories for our full radiative transfer simulations in very good agreement with a wide range of available observational constraints derived from Ly $\alpha$  forest data: mean ef-



fective optical depth, mean free path of ionising photons, incidence of LLSs, photoionisation rates.

- To reach good agreement with the rather flat evolution of inferred photoionisation rates at  $2 < z < 6$  required, however, a moderate re-scaling of the evolution of the ionising emissivity with redshift compared to the HM2012 model. The HM2012 model tends to have a too steep redshift evolution of the ionising emissivity in the redshift range  $3 < z < 6$ , while in the same range its normalisation is too low to produce the photoionisation rates inferred from Ly $\alpha$  forest data.

- In simulations that match the Ly $\alpha$  forest data well, percolation of individual HII regions occurs at  $z \sim 7$  and moderate spatial fluctuations of the photoionisation rate persist to about  $z \sim 6$ . Reionisation histories where percolation occurs sufficiently late to allow for larger spatial fluctuations of the photoionisation rate at  $z < 6$  appear to be inconsistent with the Ly $\alpha$  forest data.

- Reproducing the broad PDF of the effective optical depth in chunks of 50 comoving Mpc/h at redshift  $z \sim 5 - 6$  proved rather difficult. Spatial UV fluctuations on much larger scales ( $\gtrsim 50$  comoving Mpc/h) than produced by (sub-)  $L_*$  high-redshift galaxies appear to be required to reproduce the observed PDF of the optical depth suggesting a contribution of order unity to the ionising UV background by sources with space densities of order  $10^{-6}(\text{Mpc/h})^{-3}$ . This is very different from the widely accepted assumption made in HM2012 that the ionising emissivity at these redshifts is dominated by very faint sources, but is consistent with recent suggestions for a significant contribution of AGN to the ionising emissivity at  $z > 4$ . Such an increased contribution from faint AGN at  $z > 4$  could at the same time provide a redshift evolution of the ionising emissivity in better agreement with the redshift evolution of opacity data. Better characterising the coherence length of the spatial fluctuations of the Ly $\alpha$  optical depth at  $z > 5$  should provide valuable further information on the contribution of rare bright sources to the ionising emissivity at high redshift.

Further progress will require full radiative transfer simulations of much larger regions at a similar resolution as that of the 512-20 models discussed here that include rare bright galaxies and AGN. Another important prerequisite for further progress will be the realistic modelling of the angular and temporal distribution of the ionising radiation from starbursts and AGN including light travel time effects. Such simulations of larger regions should hopefully enable us to obtain realistic predictions of the (coupled) spatial fluctuations of mean-free path of ionising photons and photoionisation rates on the relevant large spatial scales. It will also be important to further improve the modelling of the gas distribution in galactic haloes by including stellar feedback in order to better reproduce the incidence of LLSs acting as sinks of ionising radiation.

Other avenues for improvement are multi-frequency treatment of the radiative transfer with the aim of an improved modelling of the temperature evolution of the IGM during hydrogen and helium reionisation, the self-consistent coupling of the effects of radiation pressure and the photoheating of the gas and eventually a self-consistent modelling of the ionising sources including possible self-regulating effects due to the reionisation of hydrogen.

Overall we have shown here that Ly $\alpha$  forest data provides very strong constraints on how reionisation proceeds and we expect Ly $\alpha$  forest data to become an even more important calibrator of further improved full radiative transfer simulations of the reionisation of hydrogen as we push to higher redshift with ongoing and planned QSO surveys.

## ACKNOWLEDGMENTS

We thank George Becker for making his measurements of the Ly $\alpha$  opacity PDF available before publication and James Bolton and George Becker for giving very helpful advice and comments on the manuscript. This work was supported by the ERC Advanced Grant 320596 “The Emergence of Structure during the epoch of Reionisation”. The RAMSES simulation were performed utilizing the supercomputer COSMOS Shared Memory system at DAMTP, University of Cambridge operated on behalf of the STFC DiRAC HPC Facility. This equipment is funded by BIS National E-infrastructure capital grant ST/J005673/1 and STFC grants ST/H008586/1, ST/K00333X/1. The ATON radiative transfer simulation in this work were performed using the Wilkes GPU cluster at the University of Cambridge High Performance Computing Service (<http://www.hpc.cam.ac.uk/>), provided by Dell Inc., NVIDIA and Mellanox, and part funded by STFC with industrial sponsorship from Rolls Royce and Mitsubishi Heavy Industries. DA is supported by the Agence Nationale de la Recherche Grant ANR-12-JS05-0001 “EMMA”.

## REFERENCES

- Altay G., Theuns T., Schaye J., Booth C. M., Dalla Vecchia C., 2013, MNRAS, 436, 2689
- Aubert D., Teyssier R., 2008, MNRAS, 387, 295
- Aubert D., Teyssier R., 2010, ApJ, 724, 244
- Baek S., Di Matteo P., Semelin B., Combes F., Revaz Y., 2009, A&A, 495, 389
- Bahcall J. N., Peebles P. J. E., 1969, ApJ, 156, L7
- Bauer A., Springel V., Vogelsberger M., Genel S., Torrey P., Sijacki D., Nelson D., Hernquist L., 2015, ArXiv e-prints 1503.00734
- Becker G. D., Bolton J. S., 2013, MNRAS, 436, 1023
- Becker G. D., Bolton J. S., Haehnelt M. G., Sargent W. L. W., 2011, MNRAS, 410, 1096
- Becker G. D., Bolton J. S., Madau P., Pettini M., Ryan-Weber E. V., Venemans B. P., 2015, MNRAS, 447, 3402
- Becker G. D., Hewett P. C., Worseck G., Prochaska J. X., 2013, MNRAS, 430, 2067
- Bird S., Vogelsberger M., Haehnelt M., Sijacki D., Genel S., Torrey P., Springel V., Hernquist L., 2014, MNRAS, 445, 2313
- Boera E., Murphy M. T., Becker G. D., Bolton J. S., 2014, MNRAS, 441, 1916
- Bolton J. S., Haehnelt M. G., 2007, MNRAS, 382, 325
- Bolton J. S., Haehnelt M. G., 2013, MNRAS, 429, 1695
- Bolton J. S., Haehnelt M. G., Viel M., Carswell R. F., 2006, MNRAS, 366, 1378
- Bolton J. S., Haehnelt M. G., Viel M., Springel V., 2005, MNRAS, 357, 1178



- Bolton J. S., Haehnelt M. G., Warren S. J., Hewett P. C., Mortlock D. J., Venemans B. P., McMahon R. G., Simpson C., 2011, *MNRAS*, 416, L70
- Bolton J. S., Viel M., 2011, *MNRAS*, 414, 241
- Bouwens R. J., Illingworth G. D., Franx M., Ford H., 2007, *ApJ*, 670, 928
- Bouwens R. J., Illingworth G. D., Franx M., Ford H., 2008, *ApJ*, 686, 230
- Bouwens R. J., Illingworth G. D., Oesch P. A., Trenti M., Labbé I., Bradley L., Carollo M., van Dokkum P. G., Gonzalez V., Holwerda B., Franx M., Spitler L., Smit R., Magee D., 2014, *ArXiv e-prints* 1403.4295
- Calverley A. P., Becker G. D., Haehnelt M. G., Bolton J. S., 2011, *MNRAS*, 412, 2543
- Caruana J., Bunker A. J., Wilkins S. M., Stanway E. R., Lorenzoni S., Jarvis M. J., Ebert H., 2014, *MNRAS*, 443, 2831
- Chardin J., Aubert D., Ocvirk P., 2012, *A&A*, 548, A9
- Chardin J., Aubert D., Ocvirk P., 2014, *A&A*, 568, A52
- Choudhury T. R., Haehnelt M. G., Regan J., 2009, *MNRAS*, 394, 960
- Choudhury T. R., Puchwein E., Haehnelt M. G., Bolton J. S., 2014, *ArXiv e-prints* 1412.4790
- Dijkstra M., Wyithe S., Haiman Z., Mesinger A., Pentericci L., 2014, *MNRAS*, 440, 3309
- Eisenstein D. J., Hut P., 1998, *ApJ*, 498, 137
- Emberson J. D., Thomas R. M., Alvarez M. A., 2013, *ApJ*, 763, 146
- Faisst A. L., Capak P., Carollo C. M., Scarlata C., Scoville N., 2014, *ApJ*, 788, 87
- Fan X., Strauss M. A., Becker R. H., White R. L., Gunn J. E., Knapp G. R., Richards G. T., Schneider D. P., Brinkmann J., Fukugita M., 2006, *AJ*, 132, 117
- Faucher-Giguère C.-A., Lidz A., Hernquist L., Zaldarriaga M., 2008a, *ApJ*, 682, L9
- Faucher-Giguère C.-A., Lidz A., Hernquist L., Zaldarriaga M., 2008b, *ApJ*, 688, 85
- Finkelstein S. L., Ryan Jr. R. E., Papovich C., Dickinson M., Song M., Somerville R., Ferguson H. C., Salmon B., Giallisco M., Koekemoer A. M., Ashby M. L. N., Behroozi P., Castellano M., Dunlop J. S., Faber S. M., 2014, *ArXiv e-prints* 1410.5439
- Finlator K., Özel F., Davé R., Oppenheimer B. D., 2009, *MNRAS*, 400, 1049
- Fumagalli M., O’Meara J. M., Prochaska J. X., Worseck G., 2013, *ApJ*, 775, 78
- Fumagalli M., Prochaska J. X., Kasen D., Dekel A., Ceverino D., Primack J. R., 2011, *MNRAS*, 418, 1796
- Furlanetto S. R., Mesinger A., 2009, *MNRAS*, 394, 1667
- Furlanetto S. R., Oh S. P., 2005, *MNRAS*, 363, 1031
- Giallongo E., Grazian A., Fiore F., Fontana A., Pentericci L., Vanzella E., Dickinson e. a., 2015, *ArXiv e-prints* 1502.02562
- Gnedin N. Y., 2000, *ApJ*, 535, 530
- Gnedin N. Y., 2014, *ApJ*, 793, 29
- Gnedin N. Y., Abel T., 2001, *NewA*, 6, 437
- Gnedin N. Y., Kaurov A. A., 2014, *ApJ*, 793, 30
- Haardt F., Madau P., 1996, *ApJ*, 461, 20
- Haardt F., Madau P., 2001, *Clusters of Galaxies and the High Redshift Universe Observed in X-rays*
- Haardt F., Madau P., 2012, *ApJ*, 746, 125
- Haardt F., Salvaterra R., 2015, *A&A*, 575, L16
- Hahn O., Abel T., , 2013, *MUSIC: MULTI-Scale Initial Conditions*
- Hui L., Gnedin N. Y., 1997, *MNRAS*, 292, 27
- Iliev I. T., Mellema G., Pen U., Merz H., Shapiro P. R., Alvarez M. A., 2006, *MNRAS*, 369, 1625
- Kashikawa N., Shimasaku K., Matsuda Y., Egami E., Jiang L., Nagao T., Ouchi M., Malkan M. A., Hattori T., Ota K., Taniguchi Y., Okamura S., Ly C., Iye M., Furusawa H., Shioya Y., Shibuya T., Ishizaki Y., Toshikawa J., 2011, *ApJ*, 734, 119
- Kaurov A. A., Gnedin N. Y., 2013, *ApJ*, 771, 35
- Kohler K., Gnedin N. Y., 2007, *ApJ*, 655, 685
- Konno A., Ouchi M., Ono Y., Shimasaku K., Shibuya T., Furusawa H., Nakajima K., Naito Y., Momose R., Yuma S., Iye M., 2014, *ArXiv e-prints* 1404.6066
- Lidz A., McQuinn M., Zaldarriaga M., Hernquist L., Dutta S., 2007, *ApJ*, 670, 39
- Lidz A., Oh S. P., Furlanetto S. R., 2006, *ApJL*, 639, L47
- McQuinn M., Oh S. P., Faucher-Giguère C.-A., 2011, *ApJ*, 743, 82
- Meiksin A. A., 2009, *Reviews of Modern Physics*, 81, 1405
- Mesinger A., 2010, *MNRAS*, 407, 1328
- Mesinger A., Aykutalp A., Vanzella E., Pentericci L., Ferrara A., Dijkstra M., 2015, *MNRAS*, 446, 566
- Mesinger A., Furlanetto S., 2007, *ApJ*, 669, 663
- Miralda-Escudé J., Haehnelt M., Rees M. J., 2000, *ApJ*, 530, 1
- Mortlock D. J., Warren S. J., Venemans B. P., Patel M., Hewett P. C., McMahon R. G., Simpson C., Theuns T., Gonzáles-Solares E. A., Adamson A., Dye S., Hambly N. C., Hirst P., Irwin M. J., Kuiper E., Lawrence A., Röttgering H. J. A., 2011, *Nature*, 474, 616
- Muñoz J. A., Oh S. P., Davies F. B., Furlanetto S. R., 2014, *ArXiv e-prints*
- Ocvirk P., Aubert D., Chardin J., Knebe A., Libeskind N., Gottlöber S., Yepes G., Hoffman Y., 2013, *ApJ*, 777, 51
- Ocvirk P., Gillet N., Aubert D., Knebe A., Libeskind N., Chardin J., Gottlöber S., Yepes G., Hoffman Y., 2014, *ApJ*, 794, 20
- O’Meara J. M., Prochaska J. X., Worseck G., Chen H.-W., Madau P., 2013, *ApJ*, 765, 137
- Ouchi M., Shimasaku K., Furusawa H., Saito T., Yoshida M., Akiyama M., Ono Y., Yamada T., Ota K., Kashikawa N., Iye M., Kodama T., Okamura S., Simpson C., Yoshida M., 2010, *ApJ*, 723, 869
- Pentericci L., Fontana A., Vanzella E., Castellano M., Grazian A., Dijkstra M., Boutsia K., Cristiani S., Dickinson M., Giallongo E., Giallisco M., Maiolino R., Moorwood A., Paris D., Santini P., 2011, *ApJ*, 743, 132
- Pentericci L., Vanzella E., Fontana A., Castellano M., Treu T., Mesinger A., Dijkstra M., Grazian A., Bradač M., Conselice C., Cristiani S., Dunlop J., Galametz A., Giallisco M., Giallongo E., Koekemoer A., 2014, *ApJ*, 793, 113
- Petkova M., Springel V., 2009, *MNRAS*, 396, 1383
- Planck Collaboration Ade P. A. R., Aghanim N., Armitage-Caplan C., Arnaud M., Ashdown M., Atrio-Barandela F., Aumont J., Baccigalupi C., Banday A. J., et al. 2014, *A&A*, 571, A16
- Planck Collaboration Ade P. A. R., Aghanim N., Arnaud M., Ashdown M., Aumont J., Baccigalupi C., Banday A. J., Barreiro R. B., Bartlett J. G., et al. 2015, *ArXiv*

- e-prints 1502.01589
- Prochaska J. X., Worseck G., O’Meara J. M., 2009, *ApJL*, 705, L113
- Puchwein E., Bolton J. S., Haehnelt M. G., Madau P., Becker G. D., Haardt F., 2015, *MNRAS* accepted, ArXiv e-prints 1410.1531
- Rahmati A., Pawlik A. H., Raičević M., Schaye J., 2013, *MNRAS*, 430, 2427
- Rahmati A., Schaye J., Pawlik A. H., Raičević M., 2013, *MNRAS*, 431, 2261
- Rasera Y., Teyssier R., 2006, *A&A*, 445, 1
- Rauch M., 1998, *ArAA*, 36, 267
- Rauch M., Miralda-Escudé J., Sargent W. L. W., Barlow T. A., Weinberg D. H., Hernquist L., Katz N., Cen R., Ostriker J. P., 1997, *ApJ*, 489, 7
- Razoumov A. O., Norman M. L., Abel T., Scott D., 2002, *ApJ*, 572, 695
- Rosdahl J., Blaizot J., Aubert D., Stranex T., Teyssier R., 2013, *MNRAS*, 436, 2188
- Schaye J., Dalla Vecchia C., Booth C. M., Wiersma R. P. C., Theuns T., Haas M. R., Bertone S., Duffy A. R., McCarthy I. G., van de Voort F., 2010, *MNRAS*, 402, 1536
- Sheth R. K., Mo H. J., Tormen G., 2001, *MNRAS*, 323, 1
- Songaila A., Cowie L. L., 2010, *ApJ*, 721, 1448
- Springel V., 2005, *MNRAS*, 364, 1105
- Stark D. P., Walth G., Charlot S., Clement B., Feltre A., Gutkin J., Richard J., Mainali R., Robertson B., Siana B., Tang M., Schenker M., 2015, ArXiv e-prints 1504.06881
- Telfer R. C., Zheng W., Kriss G. A., Davidsen A. F., 2002, *ApJ*, 565, 773
- Teyssier R., 2002, *A&A*, 385, 337
- Theuns T., Leonard A., Efstathiou G., Pearce F. R., Thomas P. A., 1998, *MNRAS*, 301, 478
- Trac H., Cen R., 2007, *ApJ*, 671, 1
- Trenti M., Stiavelli M., Bouwens R. J., Oesch P., Shull J. M., Ilingworth G. D., Bradley L. D., Carollo C. M., 2010, *ApJL*, 714, L202
- Treu T., Schmidt K. B., Trenti M., Bradley L. D., Stiavelli M., 2013, *ApJL*, 775, L29
- Vanden Berk D. E., Richards G. T., Bauer A., Strauss M. A., Schneider D. P., Heckman T. M., York D. G., Hall P. B., Fan X., 2001, *AJ*, 122, 549
- Viel M., Becker G. D., Bolton J. S., Haehnelt M. G., 2013, *PhRvD*, 88, 043502
- Worseck G., Prochaska J. X., O’Meara J. M., Becker G. D., Ellison S. L., Lopez S., Meiksin A., Ménard B., Murphy M. T., Fumagalli M., 2014, *MNRAS*, 445, 1745
- Wyithe J. S. B., Bolton J. S., 2011, *MNRAS*, 412, 1926

## APPENDIX A: THE HALO MASS FUNTION IN THE RAMSES SIMULATIONS

We have identified the dark matter haloes in our RAMSES simulations with the sources of ionising photons in our ATON simulations. In this appendix, we present the evolution of the halo mass function of our RAMSES simulations with different resolution and box sizes (Fig. A1). For comparison, we also plot the widely used analytical fit of Sheth et al. (2001) at each redshift which has been tested against

a wide range of numerical simulations. The halo mass function of our different simulations are in good agreement with the analytical model over the mass range where agreement should be expected. The minimum mass of haloes assumed to host ionising sources is indicated by the vertical dashed lines as well as the corresponding circular velocities.

## APPENDIX B: THE LUMINOSITY FUNCTION OF IONISING SOURCES

In our ATON simulation we have assumed that the luminosity of ionising sources scales linearly with the mass of the dark matter haloes identified in the RAMSES simulations as discussed in Appendix A. As discussed by e.g. Trenti et al. (2010) models with a linear relation between dark matter halo mass function and galaxy luminosity fit the evolution of the high-redshift luminosity function reasonably well. To test for consistency of our modelling and relate our assumed population of ionising sources to observed high-redshift galaxies we show here the evolution of the luminosity function obtained from such a linear relation between galaxy luminosity and halo mass and the halo mass functions discussed in Appendix A.

In our source model, the total comoving ionising emissivity is scaled to that in the HM2012 UV background model as described in section 2.3<sup>1</sup>. From this, we can calculate the integrated emissivity  $\epsilon_{1500}^{\text{tot}}(z)$  at 1500 Å at a given redshift. Summing over all ionising sources gives then the normalization between halo mass and 1500 Å flux  $f_{1500}$ .

Figure B1 compares the resulting luminosity functions with the observed luminosity function of high-redshift galaxies. At the highest redshifts with available data  $z \sim 9 - 8$ , there is excellent agreement of our simple model of the luminosity function and the data. At lower redshifts we somewhat overpredict the faint end of the luminosity function. Note, however, that we are interested in the hydrogen ionising luminosity for our reionisation simulations and that the escape fraction of ionising photons is generally believed to increase with decreasing galaxy luminosity. The somewhat steeper luminosity function for the ionising flux we have assumed is therefore probably as good a bet as currently possible.

## APPENDIX C: MEASURING THE MEAN FREE PATH OF IONISING PHOTONS FROM SIMULATIONS

The mean free path of ionising photons in simulations can be computed from the remaining transmission after a specific path length and by assuming that the average transmission decreases exponentially with increasing distance. A more sophisticated method is to adjust the length scale over which the transmission is measured depending on the value of the mean free path (Emberson et al. 2013).

Here we use a more direct approach which does not rely

<sup>1</sup> The comoving emissivity table of HM2012 (in  $\text{erg s}^{-1} \text{Hz}^{-1} \text{Mpc}^{-3}$ ) can be downloaded at <http://www.ucoick.org/~pmadau/CUBA>.

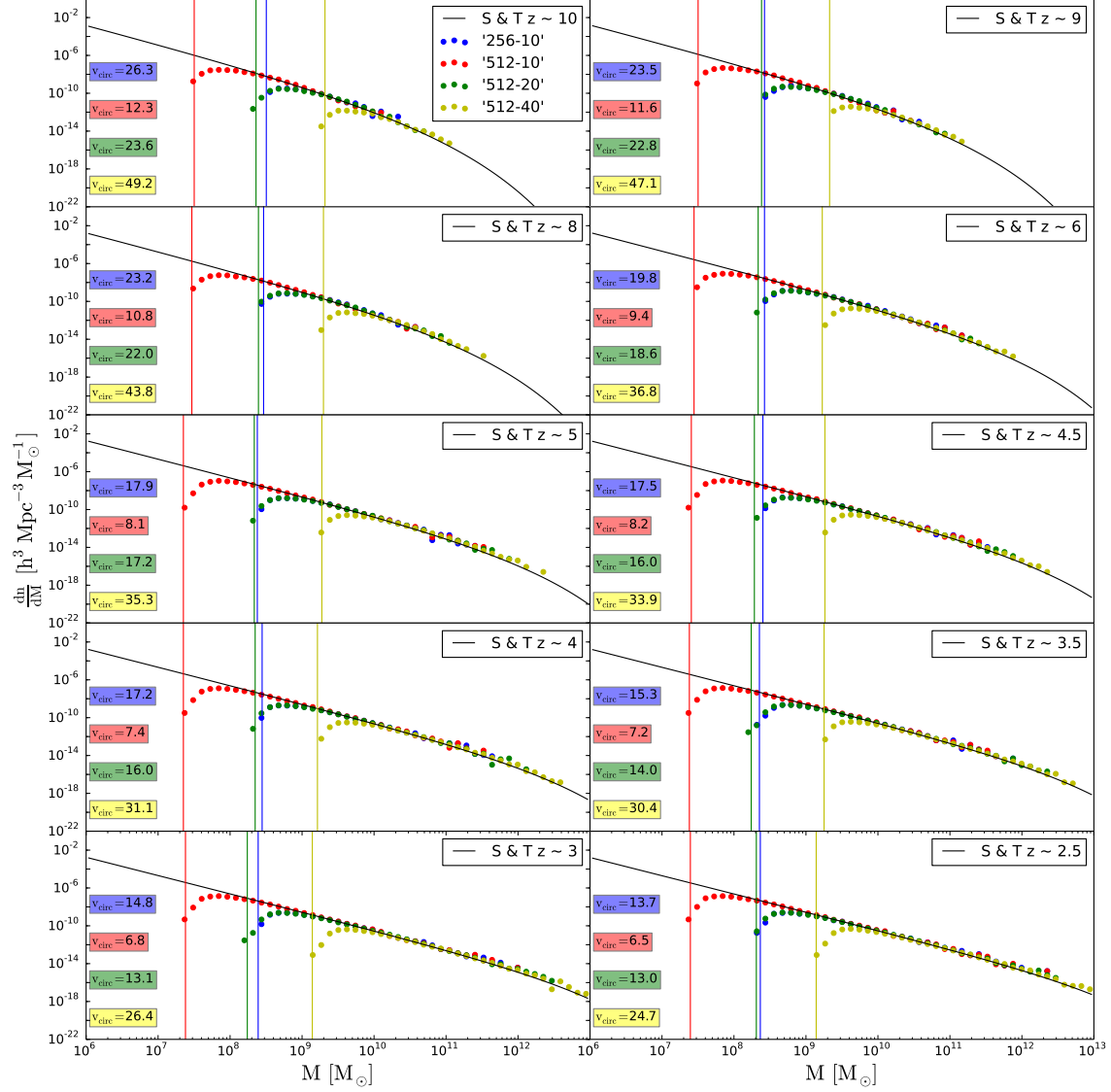


**Figure A1.** Evolution of the halo mass function in our different simulations. The analytical model of Sheth et al. (2001) is shown by the black solid curves. The coloured vertical lines show the minimum mass assumed to host ionising sources in each model. The corresponding halo minimum circular velocities are displayed on the plot (in km/s).

on choosing a length scale for the measurement or on assuming a functional form of how the transmission decreases with distance. Instead we directly use the definition of the mean free path,

$$\lambda_{\text{mfp}} = \left\langle \frac{\int x df}{\int df} \right\rangle. \quad (\text{C1})$$

Here  $f(x) = \exp(-\tau(x))$  is the transmitted ionising flux at path length  $x$  and  $\langle \dots \rangle$  denotes an average over many lines

of sight. The only assumption we need is that the neutral hydrogen density is constant within each simulation cell.

Without loss of generality we can assume that the initial ionising flux  $f(x=0) = 1$ . In this case the integral in the denominator in Eq. (C1) is equal to  $-1$ , so that we are left with

$$\lambda_{\text{mfp}} = -\left\langle \int_1^0 x df \right\rangle = \left\langle \sum_i \lambda_i \right\rangle, \quad (\text{C2})$$

where  $\lambda_i$  is the contribution of the  $i$ -th cell in the line of

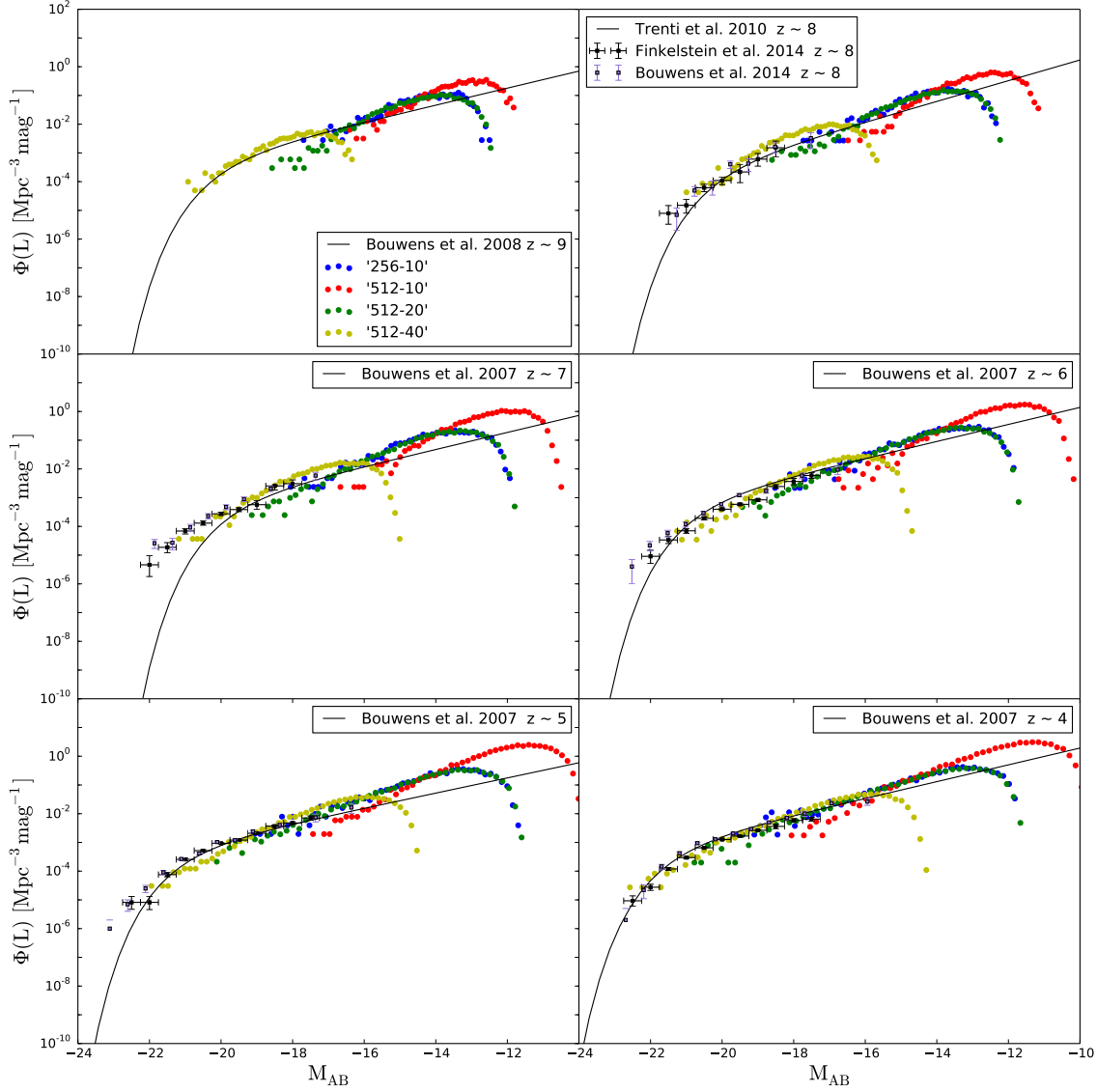


**Figure B1.** Evolution of the luminosity function in our different simulations assuming a linear relation between halo mass and 1500 Å flux as described in the text. Black and purple squares with errorbars show respectively observational constraints from Finkelstein et al. (2014) and Bouwens et al. (2014). The solid curves are fits to observational data from Bouwens et al. (2007), Bouwens et al. (2008) and Trenti et al. (2010).

sight to the integral. Next, we note that

$$-df = e^{-\tau(x)} \frac{d\tau}{dx} dx = e^{-\tau(x)} \frac{\tau_i}{\Delta x} dx. \quad (C3)$$

In the second equality, we have used the assumption that the neutral hydrogen density is constant within each cell so that  $d\tau/dx = \tau_i/\Delta x$ , where  $\tau_i$  is the optical depth of cell  $i$  and  $\Delta x$  is the cell size. Before performing the integration over cell  $i$ , we change the integration variable by defining  $l \equiv x - (i-1)\Delta x$ , which is just the distance from the beginning

of cell  $i$ . Using this we find

$$\tau(x) = \sum_{j=1}^{i-1} \tau_j + \frac{\tau_i}{\Delta x} l, \quad (C4)$$

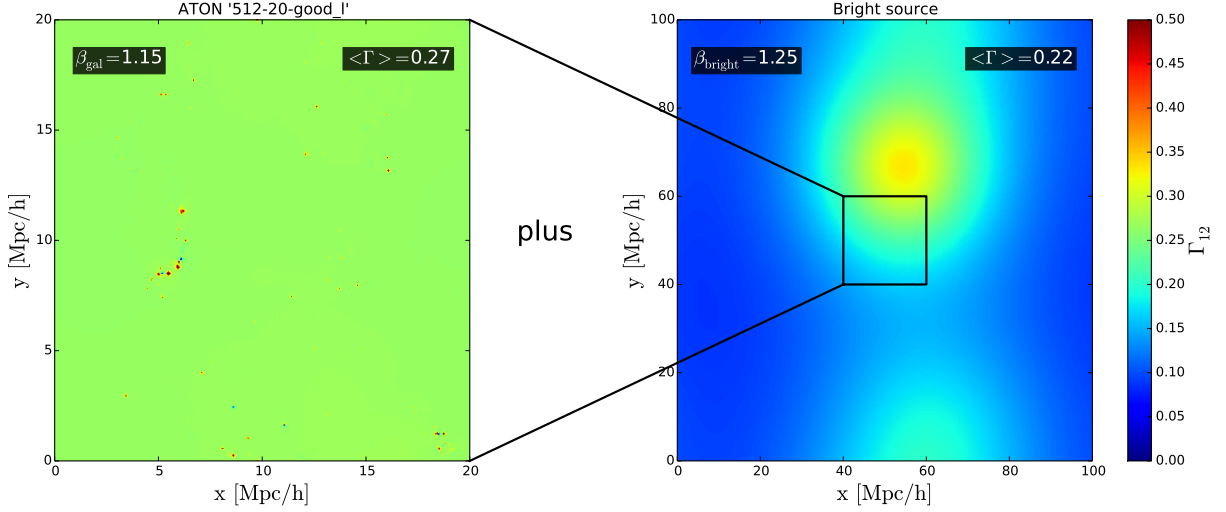


**Figure D1.** *Right:* The photoionisation rate  $\Gamma_{12}$  due to bright sources at redshift  $z \sim 5.8$  for a slice of our bright source model assuming a mean free path of  $\lambda_{\text{mfp}}^{912} \sim 35$  comoving Mpc/h and 2 bright ionising sources in the periodically replicated  $(100 \text{ Mpc/h})^3$  volume. The photo ionisation rates are normalised to match the observed cumulative Ly $\alpha$  optical depth as described in the text with  $\beta_{\text{gal}} = 1.15$  and  $\beta_{\text{bright}} = 1.25$  and the mean photoionisation rate indicated on the plot is averaged over the whole simulation box. *Left:* The photoionisation rate  $\Gamma_{12}$  in the ‘512-20-good\_l’ ATON radiative transfer model, also at redshift  $z \sim 5.8$ .

so that we can write  $\lambda_i$  as

$$\begin{aligned} \lambda_i &= e^{-\sum_{j=1}^{i-1} \tau_j} \int_0^{\Delta x} [(i-1)\Delta x + l] e^{-\frac{\tau_i}{\Delta x} l} \frac{\tau_i}{\Delta x} dl \\ &= e^{-\sum_{j=1}^{i-1} \tau_j} \left[ (1 - e^{-\tau_i})(i-1)\Delta x \right. \\ &\quad \left. + \Delta x \frac{1 - e^{-\tau_i}(1 + \tau_i)}{\tau_i} \right]. \end{aligned} \quad (\text{C5})$$

Using this expression, we find the mean free path of ionising photons along a specific line of sight by summing over the cells along it, i.e. by computing  $\sum_i \lambda_i$ . We perform this summation at least until we have reached the opposite side of the simulation box. If the transmitted flux fraction there is larger than  $10^{-8}$ , we continue the summation along another randomly chosen line of sight. We go on in this manner until  $f(x) < 10^{-8}$ . Finally, we repeat this procedure many times for different lines of sight and average the obtained mean free path values to get a global estimate of the mean free path of ionising photons.

#### APPENDIX D: A TOY MODEL FOR RARE BRIGHT GALAXIES/(FAINT) AGN

In section 3.3.4 we have argued that fluctuations of the photoionisation rate caused by rare bright galaxies or perhaps more likely (faint) AGN may be responsible of the broad Ly $\alpha$  opacity PDF measured for 50 Mpc/h chunks at  $z \sim 5.6 - 5.8$ . Here we present details of the toy model discussed there that we have used to test the effect of rare bright sources on the Ly $\alpha$  opacity PDF at redshift  $z \sim 5.8$ .

We use the location of the most massive dark matter haloes in a periodically replicated large volume simulation with a box size 100 Mpc/h on a side ( $1200^3$  particles, also used and described in Choudhury et al. 2014) at  $z \sim 5.8$  as positions for the bright ionising sources. We then compute

the photoionisation rate  $\Gamma$  due to these bright sources at every position in the 100 Mpc/h volume with the simple attenuation model used by Becker et al. (2015) (their galaxy UVB model of section 4.2, but see also Bolton & Viel 2011 and Viel et al. 2013).

We assume a spectral energy distribution appropriate for AGN for the bright sources of the form (see Vanden Berk et al. 2001 and Telfer et al. 2002),

$$L_\nu \propto \begin{cases} \nu^{-0.44} & \text{if } \lambda > 1300 \text{ \AA} \\ \nu^{-1.57} & \text{if } \lambda < 1300 \text{ \AA} \end{cases} \quad (\text{D1})$$

As a first guess we then calculate the  $L_\nu(912)$  luminosity for each source such that the total  $\epsilon_{912}$  comoving emissivity in the volume is equal to the one derived by Giallongo et al. (2015),  $2.5 \times 10^{24} \text{ erg/s/Hz/Mpc}^3$ . This results in a total ionising emissivity of  $5.18 \times 10^{56}$  and  $3.63 \times 10^{56}$  photons per seconds for the two sources. In practice the ionising emissivity as well as the corresponding fluctuations of the photoionisation rate should be dominated by objects at the knee of the luminosity function where there is currently no observational constraint at this redshift. The clustering of these sources and the enhanced mean-free path in their vicinity also plays a role. The two sources in our toy model have a space density and luminosity roughly corresponding to the region where the knee of the not yet probed QSO luminosity function at this redshift should lie. We will explore models with sources drawn from a realistic luminosity function and with a range of assumptions for their clustering in future work.

At each spatial position, we compute the specific intensity of the ionising background between 1 and 4 Ryd by summing over the contribution from each bright source,

$$J(\mathbf{r}, \nu) = \frac{1}{4\pi} \sum_{i=1}^N \frac{L_i(\mathbf{r}_i, \nu)}{4\pi |\mathbf{r}_i - \mathbf{r}|^2} e^{-\frac{|\mathbf{r}_i - \mathbf{r}|}{\lambda_{\text{mfp}}^{912}}} \left( \frac{\nu}{\nu_{912}} \right)^{-3(\beta-1)}, \quad (\text{D2})$$

where,  $\nu_{912}$  is the frequency at the HI ionising edge, and  $\beta = 1.3$  is the slope of the HI column density distribution, which gives the dependence of mean free path on frequency (see also Songaila & Cowie 2010 and Becker & Bolton 2013). The sum in equation D2 is performed for all sources within the periodically replicated simulation boxes (in practice, we included only the sources within the 100 Mpc/h box and its 26 directly neighboring periodic replications). We assume a mean free path  $\lambda_{\text{mfp}}^{912}$  as extracted from our ATON ‘512-20-good.h’ full radiative transfer simulation which has a value of  $\lambda_{\text{mfp}}^{912} \sim 35.09$  comoving Mpc/h at redshift  $z \sim 5.8$ .

The HI photoionisation rate due to bright sources is then computed as

$$\Gamma(\mathbf{r}) = 4\pi \int_{\nu_{912}}^{4\nu_{912}} \frac{d\nu}{h\nu} J(\mathbf{r}, \nu) \sigma_{\text{HI}}(\nu), \quad (\text{D3})$$

where  $\sigma_{\text{HI}}(\nu)$  is the photoionisation cross-section (calculated from the fit of Hui & Gnedin 1997).

We combine the photoionisation rates due to bright sources in our toy model as follows with the ionising UV background due to the much more numerous galaxies driving reionisation in our ATON simulations to calculate the expected effect of bright sources on the Ly $\alpha$  opacity PDF.

- We randomly choose a line-of sight through the  $100(\text{Mpc}/h)^3$  volume (along one of the principal axis) for which we have modelled the contribution of bright sources to the photoionisation rate  $\Gamma_{\text{bright}}$ .
- We concatenate three randomly selected line-of-sights from the ‘512-20-good.l’ full radiative transfer simulation and place them along the line-of-sight through the bright source model and call the photoionisation rates due to the sources in the radiative transfer simulation  $\Gamma_{\text{gal}}$ .
- We calculate the combined photoionisation rates along the line-of sight,  $\Gamma_{\text{gal} + \text{bright}} = \beta_{\text{gal}}\Gamma_{\text{gal}} + \beta_{\text{bright}}\Gamma_{\text{bright}}$ .
- The value of  $\beta_{\text{bright}}$  is calculated such that for chosen values of the number of bright sources and  $\beta_{\text{gal}}$  (the two additional free parameter of our model once a mean free path has been chosen), the mean value of the total photoionisation is that required to best match the Ly $\alpha$  opacity PDF. Note that when we calculate  $\langle \Gamma_{\text{gal} + \text{bright}} \rangle$ , we do so for the entire 100 Mpc/h cube in order to have the same value of  $\beta_{\text{bright}}$  in each line of sight.

For each model for the spatial fluctuations of the photoionisation rates we calculate 5000 mock Ly $\alpha$  spectra for 50 Mpc/h chunks as in the observed sample of Becker et al. (2015) using the density, temperature, and peculiar velocity fields from the ‘512-20-good.l’ model. We have then varied the number of bright sources and  $\beta_{\text{gal}}$  with the aim of matching the observed Ly $\alpha$  opacity PDF. In practice for a chosen number of bright sources we have started with choosing  $\beta_{\text{gal}} = 1$  and determined the value of  $\beta_{\text{bright}}$  required to match the mean photoionisation rate in the ‘512-20-good.h’ model at  $z = 5.8$  which is reasonable close to that required to match the observed Ly $\alpha$  opacity PDF. We have then further moderately rescaled  $\Gamma_{\text{gal} + \text{bright}}$  to match the observed Ly $\alpha$  opacity PDF as well as possible.

The model discussed in section 3.3.4 for which we were able to obtain a good match had two bright sources,  $\beta_{\text{gal}} = 1.15$  and  $\beta_{\text{bright}} = 1.25$ , but there will certainly be other parameter choices that will equally well reproduce the data.

In this model the galaxies driving reionisation and the bright sources responsible for the large scale fluctuations contribute about equally to the integrated ionising UV background. In figure D1, we show the photoionisation rate  $\Gamma_{\text{bright}}$  in a slice of the  $100(\text{Mpc}/h)^3$  volume for this model. For comparison, we also show a map of a slice of  $\Gamma_{\text{gal}}$ . As expected our toy model produces of order unity fluctuations of  $\Gamma$  on scales of  $\gtrsim 50$  Mpc/h, while the spatial fluctuations due to the much more abundant galaxies in our radiative transfer simulations occur on much smaller scales.

It should, however, be kept in mind that the model presented here neglects many aspects which will be important for an accurate modelling of the effect of bright sources. We have e.g. not self-consistently modelled the effect of the bright sources on the mean-free path of ionising radiation. The large spatial extent over which individual bright sources dominate also means that light-travel time effects become important if the sources are short-lived as is likely for bright starbursts and AGN. The angular distribution of the emitted ionising radiation is also likely to be not isotropic. We should thus emphasise here that the results regarding the Ly $\alpha$  opacity PDF based on this simple model should just be seen as proof of concept.